Chaos, Solitons and Fractals 195 (2025) 116262

Contents lists available at ScienceDirect

Chaos, Solitons and Fractals

journal homepage: www.elsevier.com/locate/chaos

Exploring non-Maxwellian distributions effects on modulational instability and rogue wave triplets in ion-acoustic plasmas

Abdullah Khan [a,*], Aamir Farooq [b], A.A. Abid [c], Malik Sadam Hussain [d], Wen-Xiu Ma [b,e,f], Shaaban M. Shaaban [g,*]

[a] Department of Physics, Zhejiang Normal University, Jinhua 321004, PR China
[b] Department of Mathematics, Zhejiang Normal University, Jinhua 321004, PR China
[c] Department of Physics, Qilu Institute of Technology, Jinan, 250200, Shandong, PR China
[d] Department of Engineering and Applied Physics, University of Science and Technology of China, Hefei, PR China
[e] Department of Mathematics and Statistics, University of South Florida, Tampa, FL 33620-5700, USA
[f] Material Science Innovation and Modeling, North-West University, Mafikeng Campus, Private Bag X2046, Mmabatho 2735, South Africa
[g] Center for Scientific Research and Entrepreneurship, Northern Border University, Arar 73213, Saudi Arabia

ARTICLE INFO

Keywords:
Nonlinear Wave Interactions
Nonlinear Schrödinger equation
Generalized (r,q) distribution function
Envelope solitons
Nonthermal electrons

ABSTRACT

This study explores the implications of non-Maxwellian electron distributions on modulational instability and the formation of ion-acoustic rogue wave triplets in unmagnetized collisionless plasma. We employ the reductive perturbation technique to derive the nonlinear Schrödinger equation from a fluid model that incorporates these non-Maxwellian electron distributions. This framework enables a comprehensive analysis of the modulational instability of ion-acoustic waves, characterized by the ratio of dispersion and nonlinear coefficients within the nonlinear Schrödinger equation. The injection of nonthermal electrons and spectral indices via q_n-nonextensive nonthermal and generalized (r,q) distribution functions significantly influences the onset of modulational instability and its corresponding growth rate, providing critical insights into the dynamic behavior of the plasma system. These distribution functions facilitate the identification of dark and bright solitons in stable and unstable regions, respectively. Furthermore, we incorporate multiple physical free parameters that affect the formation of rogue wave triplets. Remarkably, our findings reveal that these parameters in the second-order rogue wave solution lead to three distinct peaks arranged in a triangular pattern accompanied by a novel rotation of these peaks. We have thoroughly investigated the existence regions of both dark and bright envelope solitons, which correspond to the modulationally unstable and stable regimes of ion-acoustic waves, respectively. Our study explores into the criteria that govern the formation of these solitons, elucidating their unique features in the context of the stability dynamics of the plasma's wave system. This systematic analysis enhances our understanding of the properties of ion-acoustic solitary waves that may arise in non-Maxwellian space plasmas, paving the way for future research in this area.

1. Introduction

The phenomenon of modulational instability (MI) (so-called Benjamin–Feir Instability) emerges from the interplay between the nonlinear self-interaction and linear dispersion or diffraction of the wave configurations. This fundamental mechanism facilitates the amplification of perturbations on a continuous wave backdrop. MI has garnered significant attention across various fields, including nonlinear optics [1], fluid dynamics [2], plasma physics [3], Bose–Einstein condensates [4], and deep water waves [5]. Nonetheless, investigating MI in ion-acoustic waves (IAWs) has remained a prominent topic in plasma physics. The nonlinear Schrödinger equation (NLSE) describes the underlying mechanism of MI, which generates localized pulses through the slow variation of a monochromatic plane wave. Moreover, the MI and soliton formation governed by the NLSE have drawn significant conclusions because of their stable wave propagation. The first experimental study of MI in monochromatic IAWs was carried out by Watanabe [6]. MI has been a key area of study, with its occurrence being explored in dispersive and nonlinear plasma systems for various wave modes. This dispersive and nonlinear media have long been recognized for wave energy localization.

Numerous theoretical investigations have explored the MI for different types of wave modes. For instance, the MI of IAWs with thermally

* Corresponding authors.
E-mail addresses: abdullah@ustc.edu.cn (A. Khan), shabaan27@gmail.com (S.M. Shaaban).

https://doi.org/10.1016/j.chaos.2025.116262
Received 8 October 2024; Received in revised form 21 February 2025; Accepted 2 March 2025

adiabatic ions in a collisionless electron-positron-ion (e–p–i) plasma was reported by Chawla et al. [7]. Moreover, Jain and Mishra [8] explored the propagation of IAWs with large amplitude in a collisionless plasma containing the thermally adiabatic ions, isothermal positrons, and electrons with two temperature distributions. However, the nonlinear amplification of modulated electrostatic waves in pair plasmas was explained by Kourakis et al. [9] through a fluid model. Nejoh [10] explored the large-amplitude ion-acoustic waves in an e–p–i plasma, focusing on ion temperature effects. Numerous studies have been conducted to examine the propagation of IAWs with q_n-nonextensive electrons and positrons by utilizing the bifurcation process of planar dynamical systems, as seen in Ghosh et al. [11]. They found that both solitary and periodic waves exist, with a solid connection to the physical parameters involved. The research by Tiwari et al. [12] supported this study by examining the effects of cold ions, hot electrons, and positrons in forming ion-acoustic dressed solitons in a plasma. Saha et al. [13] studied the dynamical structures of IAWs in e–p–i magnetoplasmas with superthermal electrons and positrons, observing two- and three-solitons propagation using the Hirota direct method on the Kadomtsev–Petviashvili equation. Moreover, the oblique propagation of IAWs and the emergence of envelope soliton were further investigated by Jehan et al. [14]. They have found that the presence of positrons alters the stability regions for small propagation angles relative to the propagation direction. IAWs in unmagnetized and collisionless plasma systems serve an important role in the research of rogue wave phenomena.

Rogue waves have gained significant attention in the scientific community due to their sudden emergence occurring in the extreme ocean waves [5,15–17]. A more plausible mechanism for the formation of strongly localized rogue waves is the MI of weakly nonlinear monochromatic waves, which was first discovered in water waves [18]. This instability is best described by the NLSE [19], which governs the dynamics of wave trains in both time and space in waters of finite and infinite depths [5]. The hierarchy solutions localized in both time and space is found within the exact breather solutions on a finite background, amplifying the carrier wave's amplitude by a factor of 3 and beyond [20,21]. Solutions exhibiting these features are considered well-suited to describe the formation of rogue waves [22–24]. The Peregrine breather soliton, long been debated in the scientific community [5,15], was experimentally observed in fiber optics [25]. It was later detected in a water-wave tank [26], and subsequently observed in multicomponent plasma [27]. These findings confirmed the effectiveness of the nonlinear approach in describing the rogue waves. Furthermore, this nonlinear approach predicts not only the fundamental Peregrine soliton but also an infinite sequence of higher-order breather solutions, each with an increasingly more significant amplitude [20,21], all of which are localized in both space and time.

Various advanced methods have been employed to derive solutions for the NLSE and analyze their physical implications. These techniques include the Hirota bilinear method, the Darboux transformation, the inverse scattering transform, the Krylov–Bogoliubov–Mitropolsky approach, and the reductive perturbation method (RPT), among others [5, 28–31]. The RPT fundamentally reinterprets the spatial and temporal scales [32] for the governing equations of systems that model the long-wavelength scenarios. These governing equations through the RPT are reduced to simplify nonlinear evolution equations, such as Burgers, Korteweg–de Vries (KdV) and NLS equations. Several studies have used RPT to investigate the dynamics of non-linear acoustic waves [32–34]. Hence, it is significant to identify that RPT can serve as a powerful tool analyzing small-amplitude nonlinear wave dynamics in plasma systems. One of the most widely used approaches, the multiple scales technique (applied in both space and time), typically leads to the derivation of the NLSE that governs the evolution of a slowly modulated wavepacket envelope. A key trigger mechanisms for the growth of envelope solitons is MI, as it causes a wave field that was initially continuous or weakly modulated to spontaneously produce localized wave packets or solitons. In nonlinear plasma waves, MI plays a crucial role in energy localization, leading to the emergence of bright envelope solitons. However, the dark solitons exist even in the absence of MI, while gray envelope solitary waves, which are characterized by a velocity-dependent amplitude that may arise under certain conditions. In space plasmas, Kourakis and Shukla [35] explored the oblique modulation of electron acoustic waves, signifying that these waves could become unstable and the stability criteria strongly depend on the angle θ between the modulated wave and the wave propagation directions. They further showed that various types of localized envelope excitations of electron acoustic waves can arise in the system. The high-frequency dissipative envelope soliton in the framework of fluid theory has also been investigated in nonthermal plasmas [36]. In plasma systems, multiple distribution functions have been applied to study of rogue waves within the frameworks of ion and electron acoustic waves.

Though the Maxwellian distribution applies to systems in thermodynamic equilibrium, but astrophysical and space plasma systems that possess particle distributions deviate from it due to their quasi-steady state nature. Owing to non-equilibrium phenomena, electrons and ions in reality may not follow the Maxwellian distribution [37,38]. To address non-equilibrium phenomena, Qureshi et al. [39] proposed a more suitable and all-inclusive velocity distribution, referred to as the (r, q) generalized distribution function. The parameters r and q in this distribution function correspond to high-energy particles located on the wider shoulder of the velocity curve and the superthermality detected at the tail of the velocity curve, respectively. Zaheer et al. [40] employed the (r, q) distribution to study electrostatic wave modes, while Qureshi et al. [39] used it to examine the parallel propagation of electromagnetic waves. Shah et al. [41] explored nonlinear electron acoustic waves in planetary magnetospheres using the generalized (r, q) distribution, which accommodates both compressive and rarefactive solitary waves, in contrast to Maxwellian and kappa distributions that only allow rarefactive structures. Besides the (r, q) distribution function, the q-nonextensive nonthermal distribution has been adopted for collective and nonlinear systems exhibiting long-range interactions, which are often observed in astrophysics and plasma physics [42,43]. The study by Samanta et al. [44] focused on IAWs in a two-component plasma, considering the effects of a static magnetic field and kappa-distributed electrons. They have determined that the planar dynamical systems accommodates both solitary and periodic traveling wave solutions by using bifurcation theory. In this study, the nonextensive parameter q is referred to as q_n to differentiate it from the index q in the generalized (r, q) distribution function. This study aims to reassess the MI of IAWs using the (r, q) distribution function and to compare the results with those obtained from the q_n-nonextensive nonthermal distribution. To our knowledge, the MI and the rogue wave triplets for IAWs for the generalized (r, q) distribution function and q_n-nonextensive nonthermal distribution are not explored yet.

Therefore, the purpose of this study is to offer a comprehensive analysis of MI and its corresponding growth rate for IAWs, focusing on the effects of the spectral indices of the generalized distribution function on the rogue wave triplets. In earlier studies, the Lorentzian kappa velocity distribution and nonextensive distribution functions with nonthermal character have been used to investigate the MI and first-order rogue waves of IAWs [45]. Here, we use the same set of fluid equations for stability analysis of IAWs with the (r, q) distribution function and compare the results with those obtained using the nonextensive distribution function. The stable region of MI reduces concerning the P/Q ratio due to the spectral indices of the generalized distribution function, which will be discussed later. Here, the terms P and Q are the dispersion and nonlinear terms of NLSE, respectively. Moreover, the study also yields the explicit equations for the growth rate and rogue waves associated with MI. The graphical representations of the rogue wave triplets have also been displayed.

This paper is organized as follows: Section 2 discusses the distribution functions, the derivation of the NLSE using the reductive

perturbation scheme, and the graphical representation of dark and bright solitons in terms of P/Q ratio. The derivation of the MI growth rate and its graphical representation is outlined in Section 3. The results related to the emergence of rogue waves are presented in Section 4. Section 5 provides a comprehensive overview of the envelope soliton solutions derived from the NLSE. The concluding remarks are given in Section 6.

2. Distribution functions and the governing equations

This study focuses on the propagation of nonlinear ion-acoustic solitary waves within an unmagnetized and collisionless plasma obeying the generalized (r,q) distribution and q_n-nonextensive nonthermal distribution functions. Different distribution functions have been modeled for the Earth's magnetosphere, particularly for the polar cusp [46] and the magnetosheath [47] that reveal unique features differing from Maxwellian and kappa distributions. In this context, a generalized (r,q) distribution function has been adopted, which has the following form as [48,49]:

$$f_{(r,q)}(u) = \mathcal{N}\left[1+\frac{1}{q-1}\left(\frac{u^2-2e\phi/m_e}{\Lambda v_{th}^2}\right)^{(r+1)}\right]^{-q}, \tag{1}$$

where

$$\mathcal{N} = \frac{3\Gamma[q](q-1)^{-3/(2+2r)}}{4\pi\Lambda^{3/2}v_{th}^{3/2}\Gamma[q-\frac{3}{2+2r}]\Gamma[1+\frac{3}{2+2r}]}, \tag{2}$$

$$\Lambda = \frac{3(q-1)^{-1/(1+r)}\Gamma[q-\frac{3}{2+2r}]\Gamma[\frac{3}{2+2r}]}{2\Gamma[q-\frac{5}{2+2r}]\Gamma[\frac{5}{2+2r}]}, \tag{3}$$

where $v_{th}(=\sqrt{2T_e/m_e})$, Γ, e, ϕ stand for the thermal velocity, the gamma function, the electronic charge, and the electrostatic potential, respectively. The variables m_e and T_e in v_{th} correspond to the electron mass and temperature. To ensure that the velocity distribution function (1) is a real and positive function, the constraints $q(r+1) > 5/2$ and $q > 1$ must hold. Integrating (1) in the velocity space yields the electron density as:

$$n_e = 1 + C_1\Psi + C_2\Psi^2 + C_3\Psi^3, \tag{4}$$

where $\Psi = e\phi/T_e$ corresponds to the normalized electrostatic potential and

$$C_1 = \frac{(q-1)^{\frac{-1}{1+r}}\Gamma[q-\frac{1}{2+2r}]\Gamma[\frac{1}{2+2r}]}{2\Lambda\Gamma[\frac{3}{2+2r}]\Gamma[q-\frac{3}{2+2r}]}, \tag{5}$$

$$C_2 = \frac{-(q-1)^{\frac{-2}{1+r}}\Gamma\left[q+\frac{1}{2+2r}\right]\Gamma\left[\frac{-1}{2+2r}\right]}{8\Lambda^2\Gamma\left[\frac{3}{2+2r}\right]\Gamma\left[q-\frac{3}{2+2r}\right]}, \tag{6}$$

$$C_3 = \frac{(q-1)^{\frac{-3}{1+r}}\Gamma\left[q+\frac{3}{2+2r}\right]\Gamma\left[\frac{-3}{2+2r}\right]}{16\Lambda^3\Gamma\left[\frac{3}{2+2r}\right]\Gamma\left[q-\frac{3}{2+2r}\right]}. \tag{7}$$

Equations (5–7) reduce to $C_1 = 1$, $C_2 = 1/2$, and $C_3 = 1/6$ under the conditions $q \to \infty$ and $r = 0$, retrieving the Maxwellian distribution. In the case of $q \to \kappa+1$ and $r = 0$, the kappa distribution is recovered with the parameters $C_1 = (\kappa-1/2)/(\kappa-3/2)$, $C_2 = (\kappa-1/2)(\kappa+1/2)/(2(\kappa-3/2)^2)$ and $C_3 = (\kappa^2-1/4)(\kappa+3/2)/(6(\kappa-3/2)^3)$. We focus on elucidating the importance of the (r,q) generalized distribution function and exploring its broader implications for MI and rogue wave analysis. Fig. 1 shows the distribution function plotted against the normalized velocity $u_{normalized}$ for different values of the spectral index r at fixed q. The figure shows that as r increases, the distribution becomes flatter at the peak compared to the Maxwellian distribution. While the Maxwellian distribution exhibits a Gaussian (bell-shaped) profile, the generalized distribution displays a more complex structure, often featuring heavy tails or nonthermal characteristics depending on the spectral indices. Furthermore, an increase in r broadens the shoulders of the distribution function and reduces the presence of high-energy particles. Similarly, increasing q while keeping r fixed also leads to a decrease in the distribution function at higher energy levels. This paper's main objective is to understand how the (r,q) distributed electrons and the electrons obeying the nonextensive nonthermal distribution function influence the onset of MI and rogue waves in the plasma system. The current investigation aimed to shed light on the dynamics of IAWs in nonthermal plasma environments within the framework of the fluid model with these distributions. The electrons are considered to be nonextensive and exhibit nonthermal behavior, which can be represented by the following distribution function as [45,50]:

$$f_e(u_x) = C_{q_n,\alpha}\left\{1+\alpha\left(\frac{u_x^4}{v_{te}^4}-\frac{2\phi}{T_e}\right)^2\right\}\left[1-(q_n-1)\left(\frac{u_x^2}{v_{te}^2}-\frac{2\phi}{T_e}\right)\right]^{\frac{1}{q_n-1}+\frac{1}{2}} \tag{8}$$

where $C_{q_n,\alpha}$, α, and q_n are the normalization constant, nonthermal electrons, and nonextensive parameter, respectively [45]. Moreover, Verheest [51] provided a constraint on the range of nonextensive parameter to be more relevant $1/3 < q_n < 1$. The electron density is obtained by integrating the distribution function in (8) over the velocity space as follows [45]:

$$n_e(\phi) = \left\{1+\left(q_n-1\right)\frac{e\phi}{T_e}\right\}^{\frac{1}{q_n-1}+\frac{1}{2}}\left[1+A\left(\frac{e\phi}{T_e}\right)+B\left(\frac{e\phi}{T_e}\right)^2\right], \tag{9}$$

where the parameters $A = -16q_n\alpha/(12\alpha+15q_n^2-14q_n+3)$ and $B = 16q_n\alpha(2q_n-1)/(12\alpha+15q_n^2-14q_n+3)$. To facilitate our analysis, we define the dimensionless parameter $\Psi = e\phi/T_e$ in Eq. (9), which will play a key role in all subsequent theoretical formulations. For the derivation of NLSE using the nonextensive nonthermal electron velocity distribution, the parameters C_1, C_2, and C_3 are derived by Bouzit et al. [45]. These parameters C_1, C_2, and C_3 are distinct from the ones obtained in the (r,q) generalized distribution function.

This study focuses on the system of normalized fluid equations (i.e., continuity, momentum, and Poisson's equations) for the MI, which describe the plasma environment as:

$$\frac{\partial n_i}{\partial t}+\frac{\partial(n_iu_i)}{\partial x}=0, \tag{10}$$

$$\frac{\partial u_i}{\partial t}+u_i\frac{\partial u_i}{\partial x}=-\frac{\partial\Psi}{\partial x}, \tag{11}$$

$$\frac{\partial^2\Psi}{\partial x^2}=n_e-n_i. \tag{12}$$

here the variables $n_i(n_e)$, u_i, and Ψ correspond to the normalized ion(electron) densities, ion velocity, and electrostatic potential, respectively. The ion (electron) densities are normalized by their equilibrium values $n_{i0}(n_{e0})$, while u_i is normalized by the ion acoustic speed $C_{is}(=\lambda_{Di}\omega_{pi})$ where ω_{pi} (defined as $\sqrt{(4\pi n_0e^2/m_i)}$ and λ_{Di} (defined as $\sqrt{(T_i/4\pi n_0e^2)}$ represent the ion plasma frequency and Debye length, respectively. In this study, the temporal coordinate t and the spatial coordinate x are normalized by the inverse of ion plasma frequency (ω_{pi}^{-1}) and ion Debye length (λ_{Di}), respectively. To explore the behavior of IAWs modulation, we apply the reductive perturbation technique, which leads to the derivation of the NLSE. In this formulation, the independent variables $\xi = \varepsilon(x-v_gt)$ and $\tau = \varepsilon^2t$ are introduced, with ε as a small perturbation and v_g representing the group velocity of the wave. However, the dependent variables are expanded as

$$n_i = 1+\sum_{m=1}^{\infty}\varepsilon^{(m)}+\sum_{l=-\infty}^{\infty}n_l^{(m)}(\xi,\tau)exp[i(kx-\omega t)] \tag{13}$$

$$u_i = \sum_{m=1}^{\infty}\varepsilon^{(m)}+\sum_{l=-\infty}^{\infty}u_l^{(m)}(\xi,\tau)exp[i(kx-\omega t)], \tag{14}$$

$$\Psi = \sum_{m=1}^{\infty}\varepsilon^{(m)}+\sum_{l=-\infty}^{\infty}\Psi_l^{(m)}(\xi,\tau)exp[i(kx-\omega t)]. \tag{15}$$

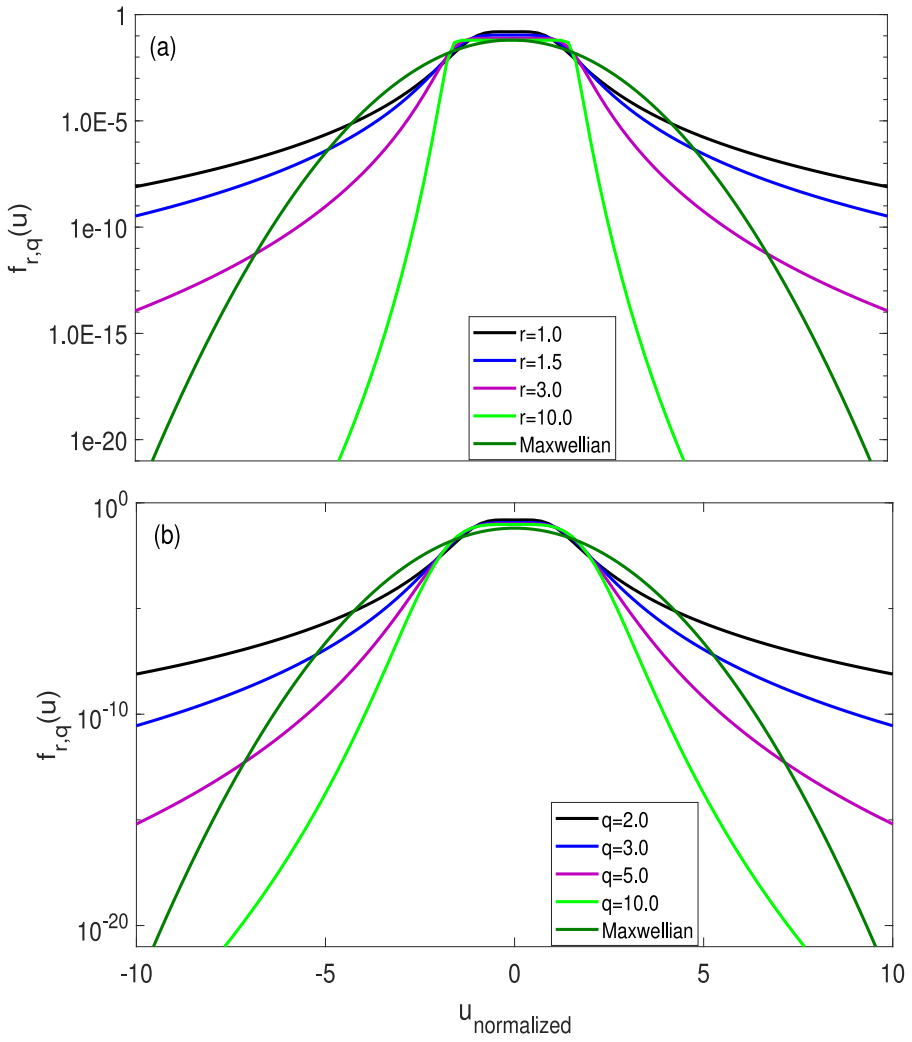

Fig. 1. Variation of the generalized (r, q) distribution function with respect to normalized velocity u for different values of (a) the spectral index r at $q = 2$ and (b) the spectral index q at $r = 1$.

The zeroth-order harmonic causes nonlinear self-interaction in carrier waves. However, the analytical calculations from the zeroth-order harmonic equations to the third-order reduced equations demonstrate the significance of nonlinear self-interaction in carrier waves. The analysis defines the dependent variables n, u, and Ψ as functions of fast (x, t) and slow (ξ, τ) coordinates to effectively separate different scales. The reductive perturbation method is employed to study the modulation of IAWs, leading to the derivation of the NLSE. For that, the independent variables are stretched as $\xi = \varepsilon(x - v_g t)$ and $\tau = \varepsilon^2 t$, where ε represents a small parameter describing the perturbation strength, and v_g is the group velocity of the wave packet. The field variables (n, u, Ψ) are expanded in powers of ε, expressed in terms of both fast $(x = \xi_0, t = \tau_0)$ and slow (ξ, τ) coordinates. Furthermore, the fast spatial and temporal coordinates are (ξ_0, τ_0), while the slow coordinates are (ξ, τ). This systematic separation effectively describes the nonlinear dynamics of the system.

The condition $A_l^m = (A_{-l}^m)^*$ must be satisfied to confirm that the physical quantities $n_p, n_n, u_{p,n}$, and Ψ remain real, where the asterisk denotes complex conjugation of the associated variable. By substituting these conditions along with the stretched coordinates into Eqs. (10)–(12) and equating terms of the same power of ϵ, the reduced equations for the mth order are derived. For instance, at the first-order approximation $(m = 1)$, the first-order quantities $n_{p1,n1}^{(1)}$, $u_{p1,n1}^{(1)}$, and $\Psi_1^{(1)}$ are obtained using Eqs. (10)–(12) as:

$$\frac{\partial n_1^{(1)}}{\partial \tau_0} + \frac{\partial u_1^{(1)}}{\partial \xi_0} = 0, \quad \frac{\partial u_1^{(1)}}{\partial \tau_0} + \frac{\partial \Psi_1^{(1)}}{\partial \xi_0} = 0, \quad \frac{\partial^2 \Psi_1^{(1)}}{\partial \xi_0^2} = C_1 \Psi_1^{(1)} - n_1^{(1)}. \tag{16}$$

The following system of equations is obtained by applying Eqs. (13)–(15) to the second-order perturbation equations of $O(\varepsilon^2)$ as:

$$\frac{\partial n_1^{(2)}}{\partial \tau_0} + \frac{\partial u_1^{(2)}}{\partial \xi_0} = v_g \frac{\partial n_1^{(1)}}{\partial \xi} - \frac{\partial u_1^{(1)}}{\partial \xi}, \tag{17}$$

$$\frac{\partial u_1^{(2)}}{\partial \tau_0} + \frac{\partial \Psi_1^{(2)}}{\partial \xi_0} = v_g \frac{\partial u_1^{(1)}}{\partial \xi} - \frac{\partial \Psi_1^{(1)}}{\partial \xi}, \tag{18}$$

$$\frac{\partial^2 \Psi_1^{(2)}}{\partial \xi_0^2} + C_1 \Psi_1^{(2)} - n_1^{(2)} = 2 \frac{\partial^2 \Psi_1^{(1)}}{\partial \xi_0 \partial \xi}. \tag{19}$$

The linear dispersion relation for IAWs is derived by solving the system in Eq. (16) through the solution $(n_1^{(1)}, u_1^{(1)}, \Psi_1^{(1)})^T = \Big([N^{(1)}(\xi, \tau), U^{(1)}(\xi, \tau), \Psi^{(1)}(\xi, \tau)]^T + \text{c.c.}\Big) \exp[i\theta]$ with $\theta = kx - \omega t$ as:

$$\frac{\omega^2}{k^2} = \frac{1}{k^2 + C_1}. \tag{20}$$

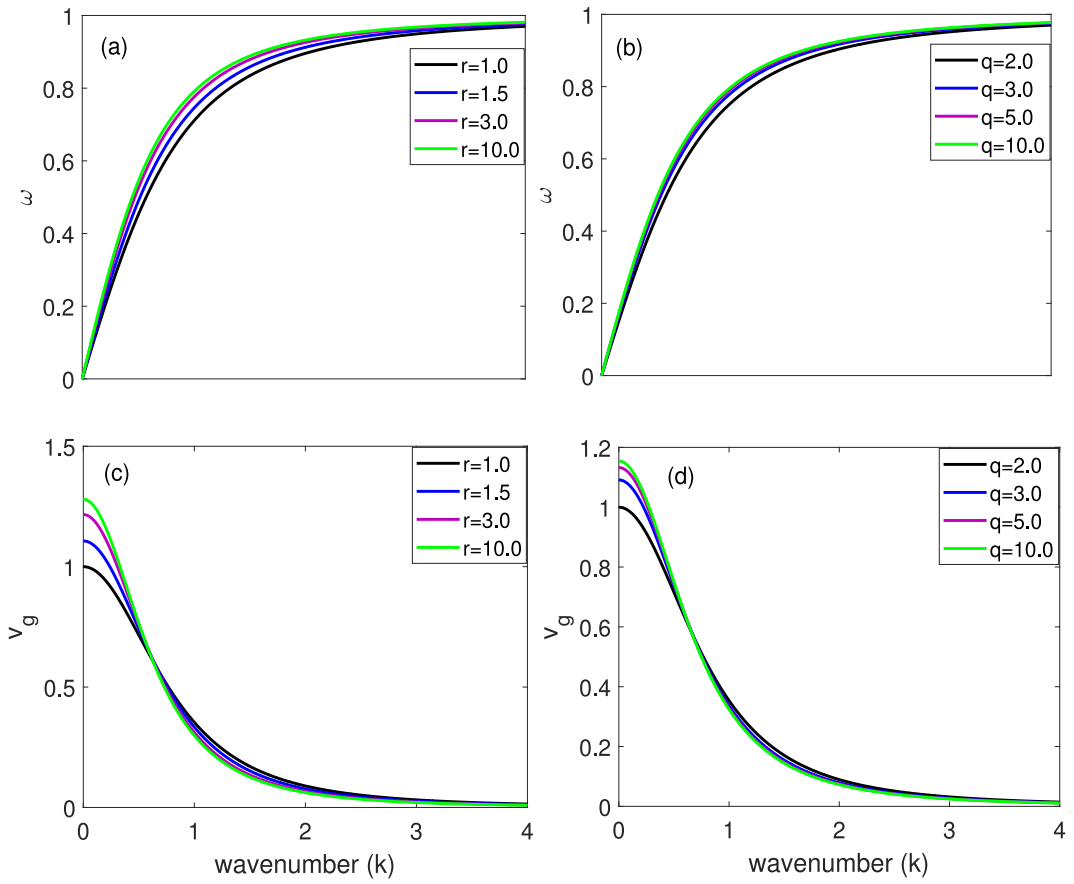

Fig. 2. Variation of the wave frequency with respect to normalized wavenumber (k) for different values of (a) the spectral index r at $q = 2$, (b) the spectral index q at $r = 1$, (c) the group velocity (v_g) for different values of r at $q = 2$, and (d) the group velocity (v_g) for different values of q at $r = 1$.

The compatibility condition is obtained from the second-order perturbation equations using Eq. (20). This modified condition offers a comprehensive framework for understanding the plasma system's behavior under perturbations and is expressed as:

$$v_g = \frac{C_1}{(k^2 + C_1)^{3/2}} \tag{21}$$

Following similar steps by applying the standard analysis (as in Ref. [45]), we derive the corresponding NLSE using the second and third order harmonic solutions as:

$$i\frac{\partial \Psi^{(1)}}{\partial \tau} + P\frac{\partial^2 \Psi^{(1)}}{\partial \xi^2} + Q|\Psi^{(1)}|^2\Psi^{(1)} = 0 \tag{22}$$

with

$$P = -\frac{3}{2}kC_1\frac{1}{(k^2 + C_1)^{5/2}}$$

$$Q = \frac{k}{2(k^2 + C_1)^{3/2}}\Big[3C_3 + 2C_2(A_\Psi + B_\Psi) - 2(k^2 + C_1)^{3/2}(A_u + B_u) - (k^2 + C_1)(A_n + B_n)\Big], \tag{23}$$

where P and Q are the dispersion and nonlinear coefficients, respectively. The variables defining these coefficients of NLSE are: $A_\Psi = (k^2 + C_1)^2/2k^2 - C_2/3k^2$, $B_\Psi = (-2C_2v_g^2 + (k^2 + 3C_1))/(C_1v_g^2 - 1)$, $A_n = (C_1 + 4k^2)A_\Psi + C_2$, $B_n = C_1B_\Psi + 2C_2$, $A_u = \omega/k[A_n - (k2 + C_1)^2]$, and $B_u = -2(k^2 + C_1)^2 \cdot \omega/k + v_gB_n$. The nonlinear propagation of IAWs gives rise to two prominent effects: (i) nonlinear frequency shift and (ii) group velocity dispersion. However, different mechanisms contribute to the nonlinear frequency shift, namely, nonlinear Landau damping, trapped electrons and ions, wave-wave coupling. These contributions have drastically different amplitude dependence because the nonlinearity coefficient in the NLSE affects the nonlinear frequency shift. Conversely, the manifestation of group velocity dispersion occurs through its corresponding coefficient in the NLSE.

In Figs. 2(a) and 2(b), the angular frequency ω is plotted over the wavenumber (k) for various values of the spectral indices of the generalized distribution function. The frequency increases with the spectral indices, as clearly illustrated by the relation $\omega^2 = k^2/(k^2 + C_1)$. Furthermore, the frequency approaches unity over a broad range of k; in Figs. 2(a) and 2(b). It is noteworthy that for higher values of the spectral indices of the generalized distribution function, the carrier frequency $\omega(k)$ exhibits a nonmonotonic trend. At large wavenumbers, the said frequency approaches unity, indicating that the wave reaches the high-frequency regime where it becomes less sensitive to further increases in k. In contrast, the group velocity behaves differently. At lower wavenumbers, specifically for $r = 1$ and $q = 2$, the group velocity is nearly one, while it decreases as the wavenumber rises. The group velocity is larger than unity as the spectral indices of the generalized distribution function increase, as illustrated in Figures 2 (c) and (d). This indicates that the wave packet slows down as the wavenumber enhances, indicating the presence of wave dissipation or damping mechanisms in the plasma.

This paper investigates the nonlinear properties of IAWs, examining the impact of various plasma parameters and the non-Maxwellian spectral indices (r, q). This study is relevant to auroral plasmas in Earth's magnetosphere, where observations suggest the presence of beam electrons that influence the IAW dynamics. To explore the possible nonlinear effects, we analyze an extreme case with $r = 5$ and $q = 10$, extending beyond the previously established ranges [39,52]. Furthermore, Williams et al. [53] restricted the range of permissible nonextensive parameters to $0.6 < q_n < 1$ in the q_n-nonextensive

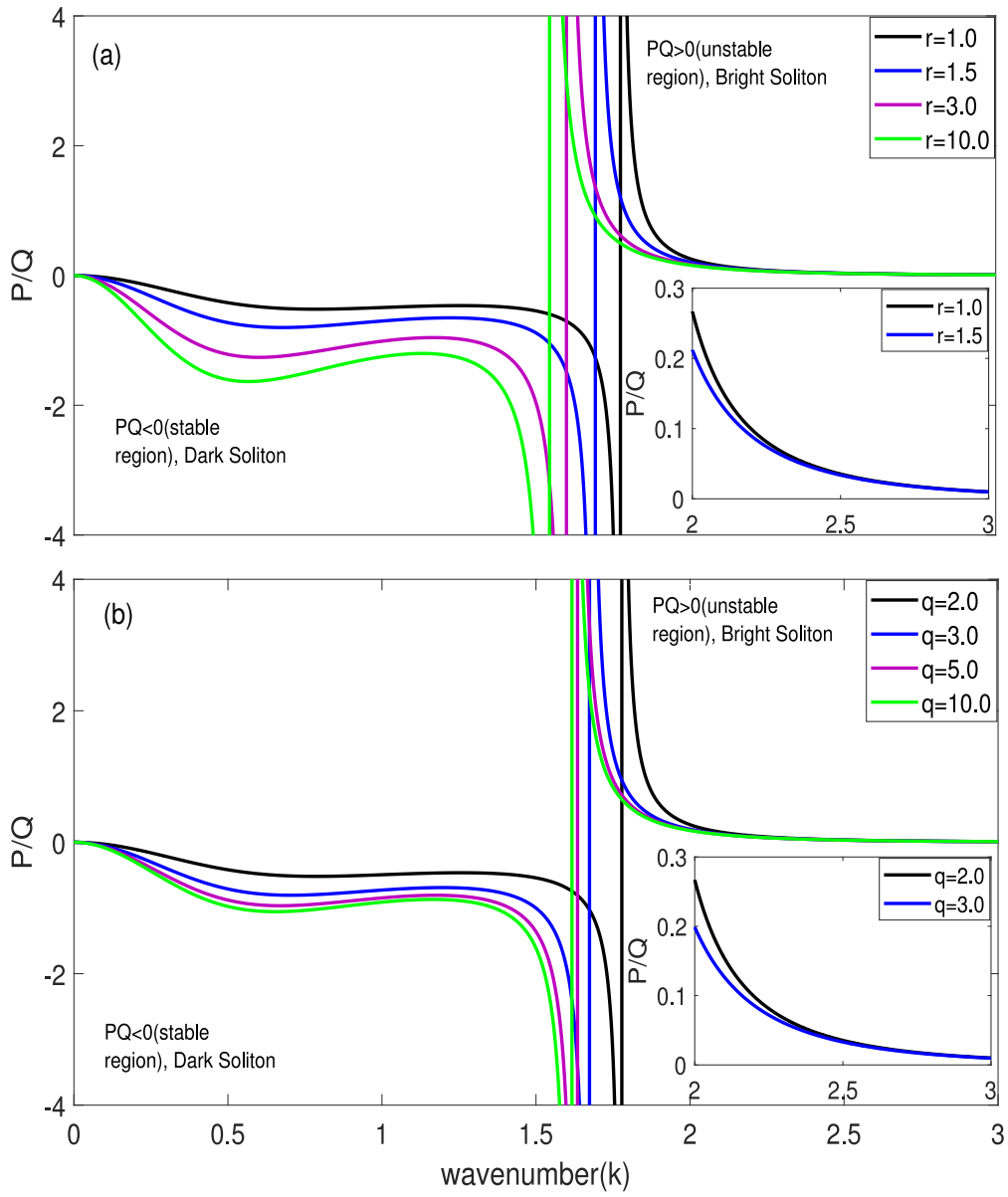

Fig. 3. Variation of the ratio P/Q with respect to normalized wavenumber (k) for different values of (a) the spectral index $r(= 1.0, 1.5, 3.0, 10.0)$ at $q = 2$ and (b) the spectral index $q(= 2.0, 3.0, 5.0, 10.0)$ at $r = 1.0$.

nonthermal distribution function. In the extensive case where $q = 1$ (the limiting case), the distribution function described in Eq. (8) reduces to the well-known Cairns distribution [54]. In this work, the nonthermal electron parameter α is comparable to the one employed by Bouzit et al. [45]. The nonlinear effects in the NLSE allow us to examine the stable/unstable regions of IAWs. However, the dispersion and nonlinear coefficients (P and Q) are the key parameters in the NLSE that influence the stable and unstable regions. The stable soliton solutions to MI are predicted by the NLSE, depending on the signs and magnitudes of P and Q [55]. For $PQ < 0$, the amplitude-modulated envelope remains unaffected by external disturbances, indicating a dark or stable soliton. The amplitude-modulated envelope becomes unstable for $PQ > 0$ due to external disturbances. The instability region promotes the collection of plasma species, leading to the formation of both bright solitons and rogue waves [56].

Based on the MI criteria, the stable and unstable regions of IAWs are distinctly identified in terms of the P/Q ratio. The stable and unstable domains are determined by the negative (positive) P/Q ratio. This further facilitates the analysis of dark and bright solitons. The negative sign of P/Q corresponds to an innately stable dark soliton. On the other hand, bright soliton is signified by the positive sign of P/Q and is either unstable or marginally unstable. The dependence of P/Q against wavenumber (k) for distinct values of the spectral indices (r, q) of the distribution function as shown in Fig. 3. The stable region of the dark soliton decreases as the spectral index r increases, as depicted in Fig. 3(a). The impact of the index r on the dark soliton becomes more prominent at the lower end of k., while its effect on the bright soliton becomes less significant at the larger end of k. The onset of instability, characterized by the critical value $k_c(= 2QP^{-1}\Psi_0^2)$ is reduced to smaller values as r intensifies. This suggests that the non-Maxwellian index r promotes the emergence of instability at large wavelengths. The threshold value for the instability is 1.75 at $r = 1$ and fixed q, which resembles the previous results by Bouzit et al. [45]. Furthermore, as illustrated in Fig. 3(a), the MI threshold value varies inversely with the index r. Fig. 3(b) shows the profile of P/Q ratio against k for the spectral index q at fixed $r(= 2)$. Here, dark and bright solitons can exist, defining the stable and unstable regions of the MI, respectively. The threshold value of the MI in terms of P/Q as a function of k varies inversely with q as clearly

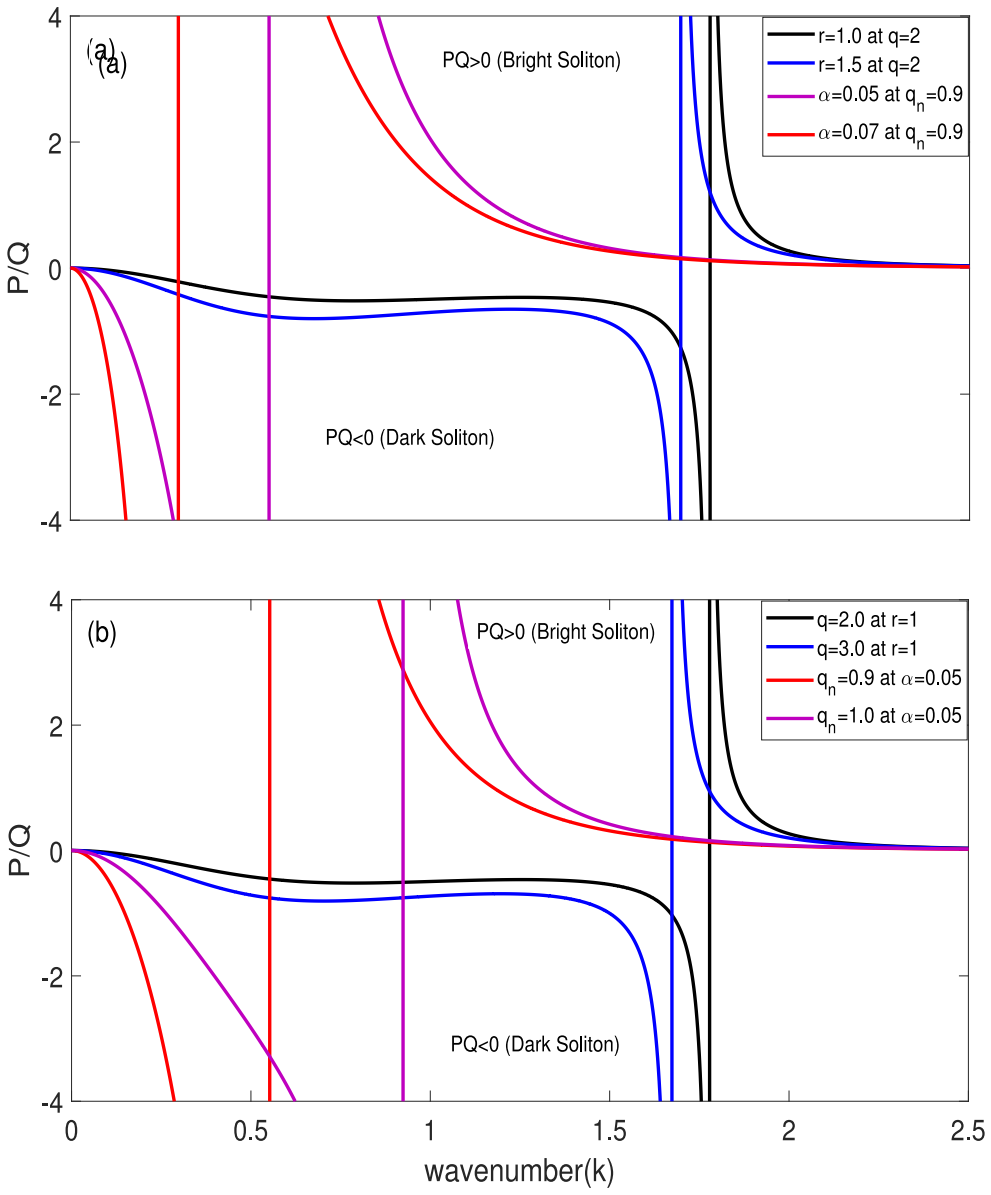

Fig. 4. Variation of the ratio P/Q for the generalized (r, q) and q_n-nonextensive distribution functions with respect to normalized wavenumber (k) for different values of (a) the spectral index $r(= 1.0, 1.5)$ at $q = 2$ and $\alpha(= 0.05, 0.07)$ at $q_n = 0.9$, and (b) the spectral index $q(= 2.0, 3.0)$ at $r = 1.0$ and $q_n = (0.9, 1.0)$ at $\alpha = 0.05$.

illustrated from Fig. 3(b). One can immediately conclude that the dark soliton is found in the region $0 < k < 1.75$, while the bright solitons is found in the region $k > 1.75$ for the different choices of the spectral indices of the generalized distribution function. The non-Maxwellian parameters exhibit only a marginal influence on the bright soliton at the higher end of k, as demonstrated by the small images in Fig. 3. Fig. 3 elucidates the effects of increasing nonlinearity (dependent on the spectral indices of the distribution function) on the stability of envelope solitons within the plasma system. As the spectral indices vary, the system undergoes a transition from a dark soliton (characterized by $P/Q < 0$) to a bright soliton regime (where $P/Q > 0$). In later scenario, an instability becomes more prominent at higher values of the spectral indices, particularly at larger wavenumbers. This indicates that enhanced nonlinearities can destabilize bright solitons, leading to more intricate wave dynamics. The transition from stable to unstable region is a key aspect of the plasma system dynamics, which confirms the possibility of rogue wave formation, where localized large-amplitude waves can suddenly appear. This shift in soliton stability indicates the strong relationship between nonlinearity and the emergence of extreme wave phenomena, such as rogue waves, which are often associated with MI.

This study also explores the influence of q_n-nonextensive nonthermal distribution on MI and compares the findings with those from the (r, q) distributed electrons, as depicted in Fig. 4. The parameter q_n can assume the value in the range of $0.6 < q_n \leq 1$ in the nonextensive nonthermal distribution, as explained by Bouzit et al. [45], whereas the parameter q is restricted from being one in the generalized distribution function presented by Shabbir et al. [49]. Both distribution functions identify the stable (unstable) regions, represented by negative (positive) values of the P/Q ratio, respectively. The $P/Q < 0$ region is conducive to dark solitons, while the $P/Q > 0$ region is indicative of bright solitons. It is found that the q_n-nonextensive nonthermal distribution significantly impacts the dark and bright soliton compared to the (r, q) distribution function as shown in Fig. 4(a). For the case $\alpha = 0.05$, the onset of instability using the q_n-nonextensive nonthermal distribution is dramatically smaller than that found with the spectral index (r) of the generalized distribution function. However, the inclusion of minimum nonthermal electrons $(\alpha = 0.07)$ significantly reduces the onset of

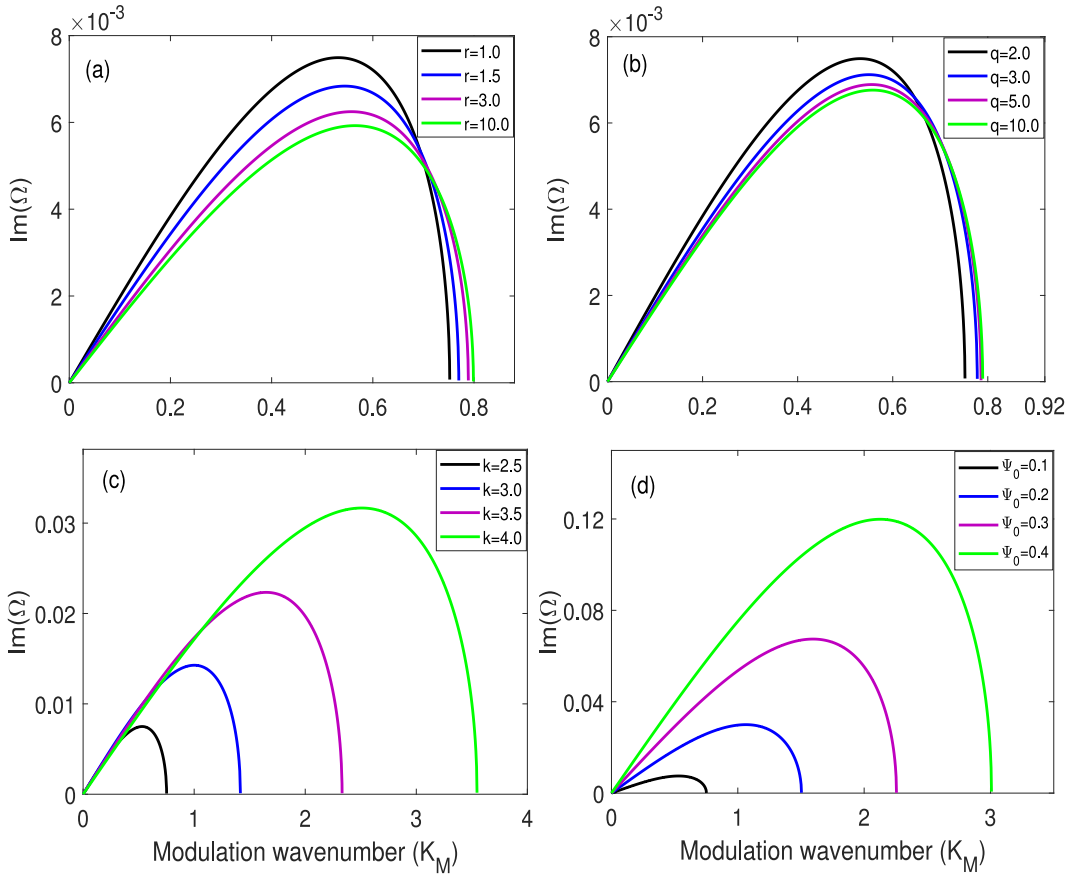

Fig. 5. Variation of the MI growth rates with respect to modulation wavenumber (K_M) for different values of (a) the spectral index r at $q = 2$, $\Psi_0 = 0.1$, and $k = 2.5$, (b) the spectral index q at $r = 1$, $\Psi_0 = 0.1$, and $k = 2.5$, (c) the normalized wavenumber k at $r = 1$, $q = 2$, and $\Psi_0 = 0.1$, and (d) the real amplitude Ψ_0 at $r = 1$, $q = 2$, and $k2.5$.

instability. On the other hand, the nonextensive parameter (q_n) compared to the spectral index (q) of the generalized distribution function significantly influences the stable and unstable regions as shown in Fig. 4(b). It is observed that the critical value of the MI for the nonextensive parameter ($q_n = 0.9$) at $\alpha = 0.05$ is 0.56, which is substantially smaller than that found for $q = 2$ at $r = 1$ in the generalized distribution function, as illustrated in Fig. 4(b). The analysis indicates that the q_n-nonextensive nonthermal distribution influences MI and envelope solitons more than the generalized (r, q) distribution function.

3. Stability analysis of the ion acoustic-waves

A small perturbation $\delta\Psi$ can be introduced to analyze the MI of IAWs. Despite the critical influence of obliqueness on the stability criteria, the IAWs are considered to propagate in the direction of the pump carrier waves [57,58]. For the analysis of MI of IAWs, we assume the plane wave solution as $\Psi^{(1)} = \Psi_0 exp\,(i\mathcal{K}\xi + i\varpi\tau)$, where Ψ_0, $\mathcal{K}$, and ϖ represent the constant real amplitude, the modulation wavenumber, and the real frequency, respectively. Applying this plane wave solution into the NLSE leads to the derivation of the nonlinear perturbed dispersion relation as: $\varpi = Q\Psi_0^2 - P\mathcal{K}^2$. For the analysis of MI, we introduce a small perturbation in $\Psi^{(1)}$, yielding the following form.

$$\Psi = (\Psi_0 + \delta\Psi)\exp(i\mathcal{K}\xi + i\varpi\tau) \tag{24}$$

where $\delta\Psi$ corresponds to the small perturbation in amplitude. The constant pump carrier amplitude Ψ_0 is substantially larger than its perturbed counterpart, i.e. $|\Psi_0| \gg |\delta\Psi|$. The NLSE (Eq. (22)) is further simplified by substituting Eq. (24) and omitting higher-order perturbed amplitudes, resulting in the linearized equation in $\delta\Psi$ as follows:

$$i\frac{\partial\delta\Psi}{\partial\tau} - \varpi\delta\Psi + P\left(\frac{\partial^2\delta\Psi}{\partial\xi^2} + 2i\mathcal{K}\frac{\partial\delta\Psi}{\partial\xi} - \mathcal{K}^2\delta\Psi\right) + Q\Psi_0^2(2\delta\Psi + \delta\Psi^\star) = 0 \tag{25}$$

here the asterisk signifies the complex conjugate of the $\delta\Psi$. Based on the approach described by Kengne and Liu [59], we look for solutions to Eq. (25) in the following form:

$$\delta\Psi = b_1\exp[i(K_M\xi - \Omega\tau)] + b_2^\star\exp[-i(K_M\xi - \Omega^\star\tau)], \tag{26}$$

in Eq. (26), b_1 and $b_2^\star$ are complex amplitudes, where Ω denotes the complex modulation frequency, and K_M is the real modulation wavenumber associated with the perturbations. Applying the real modulation frequency (e.g., $\varpi = Q\Psi_0^2 - P\mathcal{K}^2$) along with Eq. (26) to Eq. (25) leads to the following equation for the complex frequency (Ω) as:

$$\Omega = 2PK_M\mathcal{K} \pm iPK_M\sqrt{\frac{2Q}{P}\Psi_0^2 - K_M^2} \tag{27}$$

The dependence of the modulation frequency (Ω) on both the real modulation wavenumber K_M and the carrier wavenumber $\mathcal{K}$ is evident from Eq. (27). The imaginary component of Ω determines the stability of the IAWs. According to Eq. (27), the IAWs will be unstable under modulation if $Im(\Omega)$ is greater than zero, while they will be stable if $Im(\Omega)$ is zero or negative. It is important to note that when $2Q\Psi_0^2/P > K_M^2$, the IAWs remain unstable under modulation since their frequency is real for any admissible value of modulation wavenumber (K_M). Conversely, when $2Q\Psi_0^2/P < K_M^2$, the IAWs remain stable under modulation because the real part of the frequency is zero for any value of the modulated wavenumbers (K_M). For a positive product PQ, the frequency Ω will show a nonzero real part if the modulation of the perturbation meets the following criteria.

$$K_M^2 - \frac{2Q}{P}\Psi_0^2 < 0 \tag{28}$$

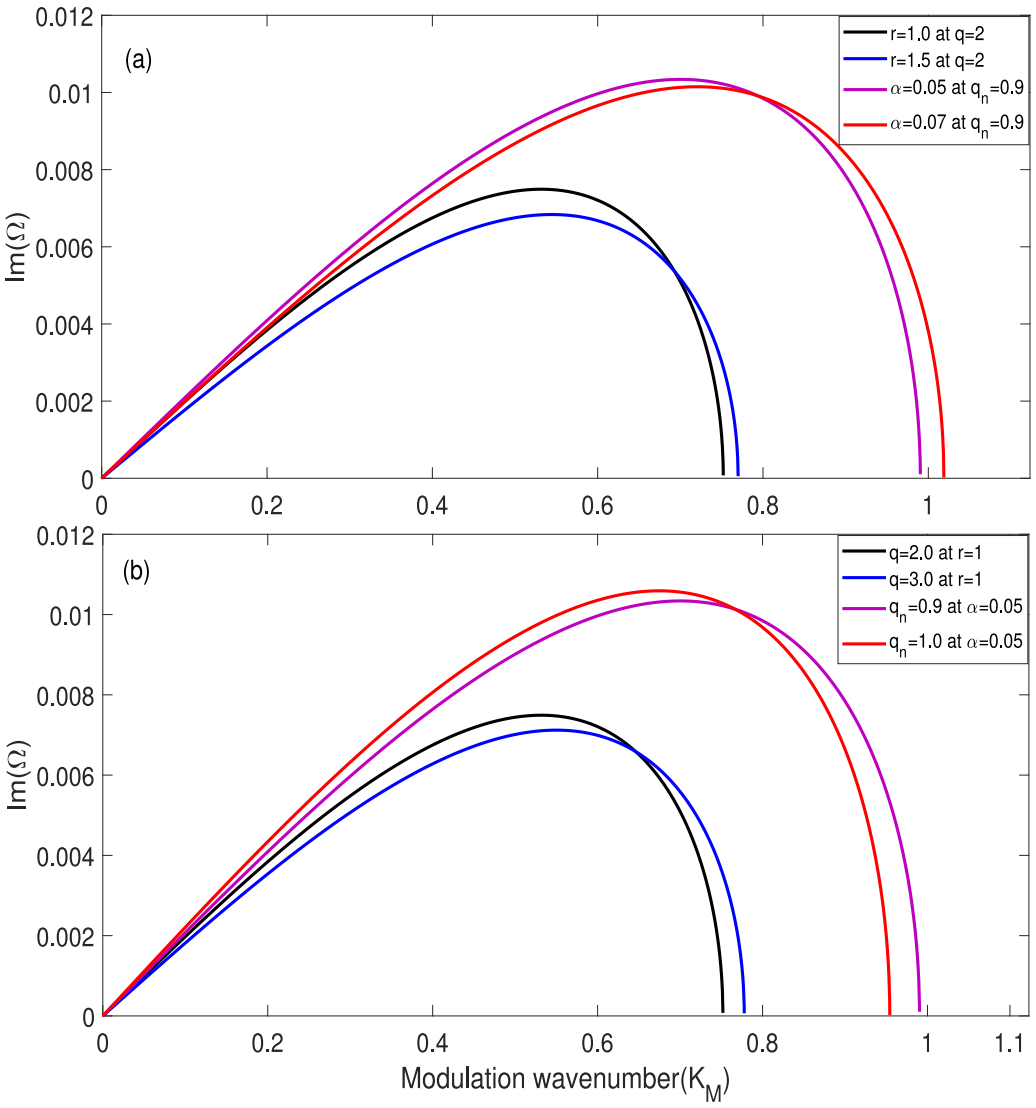

Fig. 6. Variation of the MI growth rates for the generalized (r, q) and q_n-nonextensive distribution functions with respect to modulation wavenumber (K_M) for different values of (a) the spectral index $r(= 1.0, 1.5)$ at $q = 2$ and $\alpha(= 0.05, 0.07)$ at $q_n = 0.9$, and (b) the spectral index $q(= 2.0, 3.0)$ at $r = 1.0$ and $q_n = (0.9, 1.0)$ at $\alpha = 0.05$.

Under condition (28), the equation that determines the local growth rate $Im(\Omega)$ of MI is as follows:

$$Im(\Omega) = |PK_M|\sqrt{\frac{2Q}{P}\Psi_0^2 - K_M^2} \tag{29}$$

We now analyze the stability and instability of modulated wave packets using the NLSE (22) that describes the MI of IAWs. Bains et al. [50] examined that the IAWs become unstable under modulation when $PQ > 0$. Here $PQ > 0$ is the region where K_M^2 is less than the critical wavenumber $k_c(= 2Q\Psi_0^2/P)$. The k_c defines the boundary of the instability region. Two distinct solitons can be identified: stable dark envelope solitons for region $PQ < 0$ and unstable bright envelope solitons for region $PQ > 0$. Furthermore, the spectral indices (r, q) of the generalized distribution function clearly influence the dispersion and nonlinear coefficients (P and Q), which in turn have a potential impact on the stable and unstable regions of IAWs.

We investigate the impact of the spectral indices in the generalized distribution function on the MI growth rate of IAWs in a long range of modulation wavenumbers (K_M) as shown in Fig. 5. The growth rate is evaluated in the MI region where $PQ > 0$, indicating that the dispersion and nonlinear terms have the same sign. The growth rate of MI of IAWs for various choices of the index r reaches a peak value in the middle of the modulation wavenumber. The peak value of the MI growth rate for $r = 1$ is found to be larger than that found for $r = 10$ as shown in Fig. 5(a). It is important to identify that the growth rate for $r = 10$ is fully suppressed at $K_M = 0.8$. However, the suppression effect becomes less as the value of r decreases. Furthermore, in the range $0 < K_M < 0.5$, the growth rate is enhanced due to the modulation wavenumber K_M being located outside the square root (e.g., see Eq. (29)), as shown in Fig. 5(a). As evident from Eq. (29), the MI growth rate decreases due to K_M being inside the square root. The influence of the spectral index q on the MI growth rate is depicted in Fig. 5(b). The growth rate shows the similar trend as for the spectral index r. The role of the spectral index q in the MI analysis is less prominent than that of the r, as portrayed in Fig. 5(b). This study finds that the impact of both non-Maxwellian indices on the growth rate of MI is marginal at the high end of K_M.

The MI growth rate, depicted in Figs. 5(c) and 5(d), is evaluated as a function of K_M for various choices of carrier wavenumbers k and a real constant amplitude Ψ_0. The spectral indices of the distribution function for this case are kept constant which are $(1, 2)$. It is evident from Eq. (29) that the critical wavenumber k_c significantly depends on the carrier wavenumber k, which in turn enhances the unstable region of the instability. As the carrier wavenumber k increases, the ratio Q/P also increases, thereby increasing the range of modulation wavenumber K_M. For this purpose, Fig. 5(c) demonstrates that the critical wavenumber k_c increases with the carrier wavenumber k, which

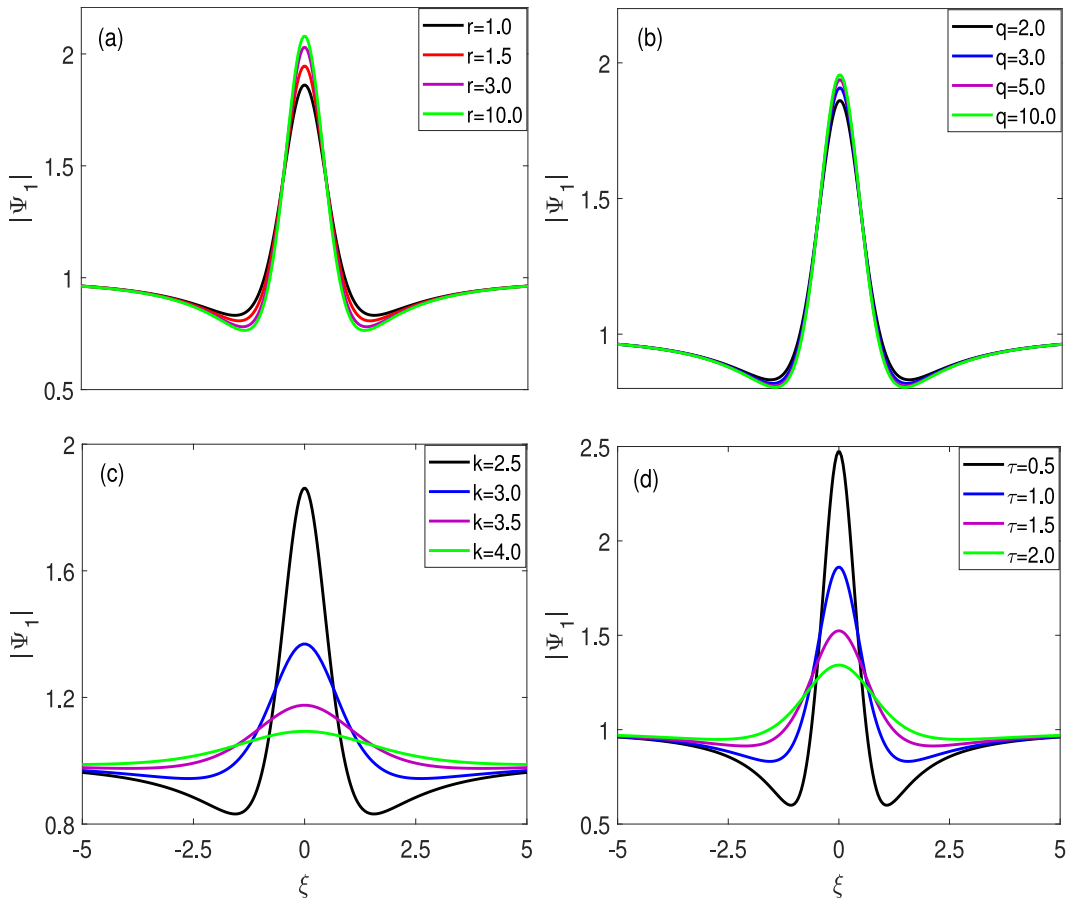

Fig. 7. The 1D behavior of the first-order rogue waves $|\Psi_1|$ with respect to ξ for different values of (a) the spectral index r at $q = 2$, $k = 2.5$, and $\tau = 0.5$, (b) the spectral index q at $r = 1$, $k = 2.5$, and $\tau = 0.5$, (c) the wavenumber k at $r = 1$ and $q = 2$, and (d) temporal coordinate τ at $r = 1$, $q = 2$, and $k = 2.5$.

enhances the instability region. Fig. 5(d) shows that the growth rate of MI increases as the constant real amplitude Ψ_0 increases. The modulation wavenumber outside the square root (e.g. see Eq. (29)) causes the growth rates to increase and reach peak values in the unstable region. This indicates that the maximum value of the growth rate becomes more prominent when the constant amplitude Ψ_0 increases. However, the growth rates are entirely suppressed when $K_M > 3$ for all amplitude values Ψ_0 due to K_M being inside the square root, as illustrated in Fig. 5(d). The increased instability at larger Ψ_0 indicates that a higher plasma potential amplifies MI. In general, MI dynamics are significantly influenced by the spectral indices of the generalized distribution function (r, q), the wavenumber k, and the plasma potential Ψ_0, as shown in Fig. 5. It demonstrates that the instability growth rate decreases with rising spectral indices r and q, indicating that higher values of these indices tend to stabilize the IAWs. Conversely, the plasma potential Ψ_0 and the carrier wavenumber enhance the instability at large modulation wavenumber.

The nonextensive nonthermal velocity distribution, characterized by the parameters q_n and α, reflects the effects of nonextensive and nonthermal electrons on MI, while the parameters r and q serve as the spectral indices in the generalized distribution function. We investigate the impact of q_n and α on the MI growth rate and compare it with the results obtained from the generalized distribution function, as shown in Fig. 6(a). In Fig. 6(a), the growth rate observed for the parameters q_n and α is higher than that of the generalized distribution parameters. Compared to the generalized distribution, the MI growth rate in the nonextensive velocity distribution is nearly 0.004 times larger. Moreover, the influence of the parameters q_n and α on the MI growth rates is more significant than that of the spectral indices r and q. The injection of nonthermal electrons (α) into the plasma system expands the instability region of IAWs, as illustrated in Figure 6(a). In the cases of $q_n = 0.9$ and $q_n = 1.0$, the MI growth rate follows an inverse trend to that for nonthermal electrons (α), as illustrated in Fig. 6(b). Compared to the generalized distribution function, the instability region of IAWs is much more significant in the nonextensive nonthermal distribution. This suggests that the scenario for the emergence of rogue wave triplets in a plasma system, as indicated by the fluid model for IAWs, is still probable in the instability region [45,50]. Compared to the q_n-nonextensive nonthermal distribution function, the generalized (r, q) distribution results in a lower growth rates in the small k region by modifying the plasma's response to long-wavelength perturbations, thereby reducing the available energy for instability at large scales. On the other hand, the nonextensive nonthermal distribution enhances the suppression of the growth rate in the large k regime, indicating a stronger damping effect on the instability at short wavelengths. These distributions play distinct roles in the dynamics of MI in plasmas, with the generalized (r, q) distribution stabilizing long-wavelength modes and the nonextensive nonthermal distribution damping short-wavelength modes.

4. Formation of rogue wave triplets

The emergence of rogue waves of IAWs in a dispersive plasma medium is described by the NLSE (Eq. (22)). This equation is a partial differential equation that illustrates the effects of both dispersion and nonlinearity. Furthermore, this equation admits numerous types of solutions, namely breathers, rogue waves, rogue wave triplets, dark and bright solitons. These solutions are contingent upon the features of plasma and their initial conditions. The NLSE provides infinitely numerous exact breather solutions for Ψ, localized in space and time

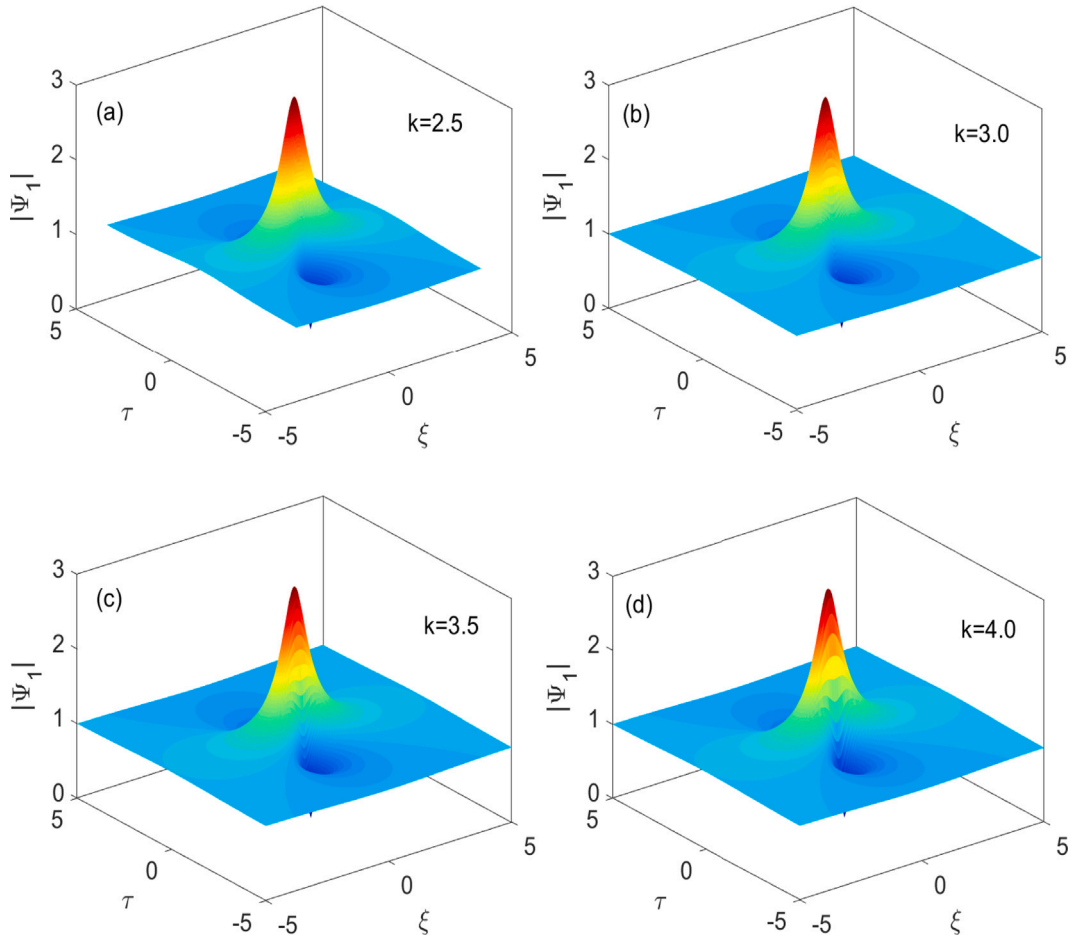

Fig. 8. The 3D behavior of the first-order rogue waves $|\Psi_1|$ with respect to ξ and τ for (a) $k = 2.5$, (b) $k = 3.0$, (c) $k = 3.5$, and (d) $k = 4.0$ at $r = 1$ and $q = 2$.

in the modulationally unstable region where $PQ > 0$. The growth of random amplitude perturbations in the $PQ > 0$ region leads to the emergence of rogue waves. The rational solution of Eq. (22) for the rogue wave in the $PQ > 0$ region can be obtained using the Darboux transformation scheme for both time and space as follows [60,61]:

$$\Psi_n(\xi,\tau) = \left[(-1)^n + \frac{G_n(\xi,\tau) + iK_n(\xi,\tau)}{D_n(\xi,\tau)}\right] exp(iQ\tau), \tag{30}$$

where G_n, K_n, and D_n are functions related to the order n of the solution. To ensure the solution remains finite everywhere, the denominator D_n must not have any zeros. The first-order rogue wave solution of Eq. (22) is given as [60,61]:

$$\Psi_1(\xi,\tau) = \left[-1 + 4\frac{1 + 2iQ\tau}{1 + 4(Q\tau)^2 + 4\left(\sqrt{\frac{Q}{2P}}\xi\right)^2}\right] exp(iQ\tau), \tag{31}$$

The second-order rogue wave solution of Eq. (22) is given as [60,61]

$$\Psi_2(\xi,\tau) = \left[1 + \frac{G_2(\xi,\tau) + iK_2(\xi,\tau)}{D_2(\xi,\tau)}\right] exp(iQ\tau), \tag{32}$$

with

$$\begin{aligned} G_2 = 12\Bigg[& 3 - 16\left(\sqrt{\frac{Q}{2P}}\xi\right)^4 - 24\left(\sqrt{\frac{Q}{2P}}\xi\right)^2\left(4(Q\tau)^2 + 1\right) \\ & - 4\beta\left(\sqrt{\frac{Q}{2P}}\xi\right) \\ & -80(Q\tau)^4 - 72(Q\tau)^2 + 4\gamma(Q\tau)\Bigg], \end{aligned} \tag{33}$$

$$\begin{aligned} K_2 = 24\Bigg[& Q\tau\left\{15 - 16\left(\sqrt{\frac{Q}{2P}}\xi\right)^4 + 24\left(\sqrt{\frac{Q}{2P}}\xi\right)^2 - 4\beta\sqrt{\frac{Q}{2P}}\xi\right\} \\ & -8\left\{4\left(\sqrt{\frac{Q}{2P}}\xi\right)^2 + 1\right\}(Q\tau)^3 - 16(Q\tau)^5 \\ & +\gamma\left\{2(Q\tau)^2 - 2\left(\sqrt{\frac{Q}{2P}}\xi\right)^2 - \frac{1}{2}\right\}\Bigg], \end{aligned} \tag{34}$$

$$\begin{aligned} D_2 = & 64\left(\sqrt{\frac{Q}{2P}}\xi\right)^6 + 48\left(\sqrt{\frac{Q}{2P}}\xi\right)^4\left(4(Q\tau)^2 + 1\right) \\ & + 12\left(\sqrt{\frac{Q}{2P}}\xi\right)^2\left\{3 - 4(Q\tau)^2\right\}^2 + 64(Q\tau)^6 + 432(Q\tau)^4 + \\ & 396(Q\tau)^2 + 9 + \beta\left[\beta + 4\left(\sqrt{\frac{Q}{2P}}\xi\right)\left(12(Q\tau)^2 - 4\left(\sqrt{\frac{Q}{2P}}\xi\right)^2 + 3\right)\right] \\ & + \gamma\left[\gamma + 4(Q\tau)\left\{12\left(\sqrt{\frac{Q}{2P}}\xi\right)^2 - 4(Q\tau)^2 - 9\right\}\right]. \end{aligned} \tag{35}$$

the parameters β and γ are real constants that can be chosen arbitrarily. The solution involves D_2 as a 6th-order polynomial, while G_2 and K_2 as 4th- and 5th-order polynomials, respectively. Ankiewicz et al. [60] employed different coefficients compared to those in (e.g., see Dubard et al. [62]), owing to the precise form of the NLSE. The presence of the free parameters γ and β distinguishes these equations from those found earlier by Akhmediev et al. [21]. It was concluded by Ankiewicz et al. [60] that these solutions agree with the equations derived by Akhmediev et al. [21] when γ and β are both set to zero. The presence of non-zero parameters significantly affects the higher-order rogue wave structure. In this work, we extend the analysis of

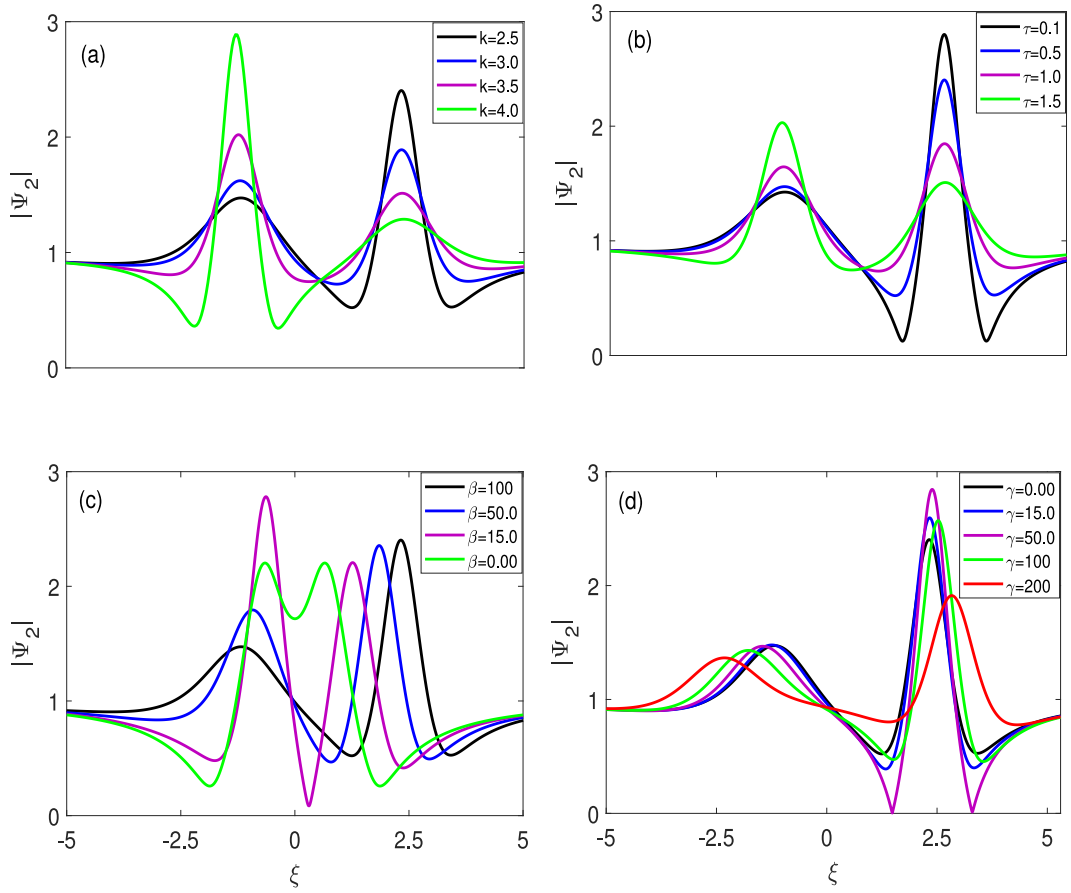

Fig. 9. The 1D behavior of the rogue wave triplets $|\Psi_2|$ with respect to ξ for different values of (a) the wavenumber k at $\tau = 0.5$, $\beta = 100$, and $\gamma = 0$ (b) the temporal coordinate τ at $k = 2.5$, $\beta = 100$, and $\gamma = 0$, (c) the physical free parameter β at $k = 2.5$, $\tau = 0.5$, and $\gamma = 0$, and (d) the physical free parameter γ at $k = 2.5$, $\tau = 0.5$, and $\beta = 100$.

Ankiewicz et al. [60] on higher-order rogue waves, referred to as rogue wave triplets, for the IAWs using the plasma fluid model. The goal of our analysis below is to identify the relative positions concerning γ and β for rogue wave triplets in the plasma system.

The substantial impacts of the spectral indices (r, q), the carrier wavenumber k, and the temporal coordinate τ on the first-order rogue waves of IAWs are explored, as depicted in Fig. 7. It is evident from Fig. 7(a) that the peak value of the rogue wave positioned at $\xi = 0$ increases with the index r at fixed $q(= 2)$ and $\tau(= 0.5)$. Since the ratio P/Q against k shows minimal variation for various values of r, therefore a similar trend of r can be seen here in the ion acoustic first-order rogue waves. Moreover, the index q also has a marginal effect on the rogue waves, as seen in Fig. 7(b). The intensity profile of the first-order rogue waves is plotted as a function of ξ for different values of the wavenumber k as shown in Fig. 7(c). The wavenumber significantly impacts the rogue waves, leading to a flattening of the amplitude of the rogue waves as the wavenumber increases. Moreover, the maximum values of the rogue wave at $\xi = 0$ drop when k surpasses 2.5, as depicted in Fig. 7(c). The temporal coordinate τ also dramatically affects the dynamics of the first-order rogue waves, as depicted in Fig. 7(d). As illustrated in Fig. 7(d), the one-dimensional (1D) profile of $|\Psi_1|$ shows that the amplitude becomes narrower at smaller values of τ, indicating a more robust localization of IAWs.

The three-dimensional (3D) visualization of the first-order rogue wave at different carrier wavenumbers k is illustrated in Fig. 8. Here the spectral indices (r, q) are constant $(1, 2)$. It can be seen from Fig. 8(a) that the rogue waves amplitude broadens at smaller values of k. This further indicates the localization of the rogue waves. Consistent with the 1D profile shown in Fig. 7(c), the amplitude of the first-order rogue waves of IAWs becomes narrower at $k = 2.5$, but widens with increasing k, as illustrated in Fig. 8.

The 1D behavior of rogue wave triplet against ξ for various values of the wavenumber k is evaluated while the spectral indices (r, q) of the distribution function, the physical free parameters (β and γ) and the temporal coordinate τ kept fixed as shown in Fig. 9. It is evident from this figure that the rogue waves exhibit two distinct peaks within the spatial coordinate range $-5 < \xi < 5$ for different values of k. The rogue wave triplets reach their peak values at two different locations, namely $\xi = -1.25$ and $\xi = 1.25$ as shown in Fig. 9(a). Notably, the rogue waves' peak intensity grows with increasing wavenumber at $\xi = -1.25$ but declines at $\xi = 1.25$, as illustrated in Fig. 9(a). As seen in Fig. 9(b), the intensity profiles of the rogue wave triplet are displayed for various values of τ in the same range of ξ $(-5 < \xi < 5)$. This figure further illustrates that the maximum values of the rogue waves, corresponding to the peaks, are located at $\xi = -1.25$ and $\xi = 1.25$. In conclusion, the rogue wave triplet exhibits a similar pattern for varying values of k and τ (see Figs. 9(a) and 9(b) for reference). The 1D profiles of the rogue wave triplets is plotted in terms of physical free parameter β. A detailed representation of the results is provided in Fig. 9(c). Here, the spectral indices (r, q) are set to $(1, 2)$, while $(k, \tau) = (2.5, 0.5)$. The two peaks are also shown for different β values while the peak intensity shifts toward zero in the region $xi < 0$ as β decreases from 100 to 50, as depicted in Fig. 9(c). Conversely, in the region $\xi > 0$, the peak intensity $(|\Psi_2|)$ shifts toward zero as the free parameter β decreases. The parameter γ also has a significant influence on the rogue wave triplet, as shown in Fig. 9(d). It is noteworthy that the variations in peak values of the intensity for different γ within the region $\xi > 0$ are more significant than those found in the region $\xi < 0$. In the region $\xi < 0$, the maximum value of $|\Psi_2|$ shifts away from zero as the parameter γ gets larger (e.g. see Fig. 9(d)).

Next, we explore the impact of the physical free parameters β and γ on the rogue wave triplets $(|\Psi_2|)$ of IAWs, with the 2D and 3D

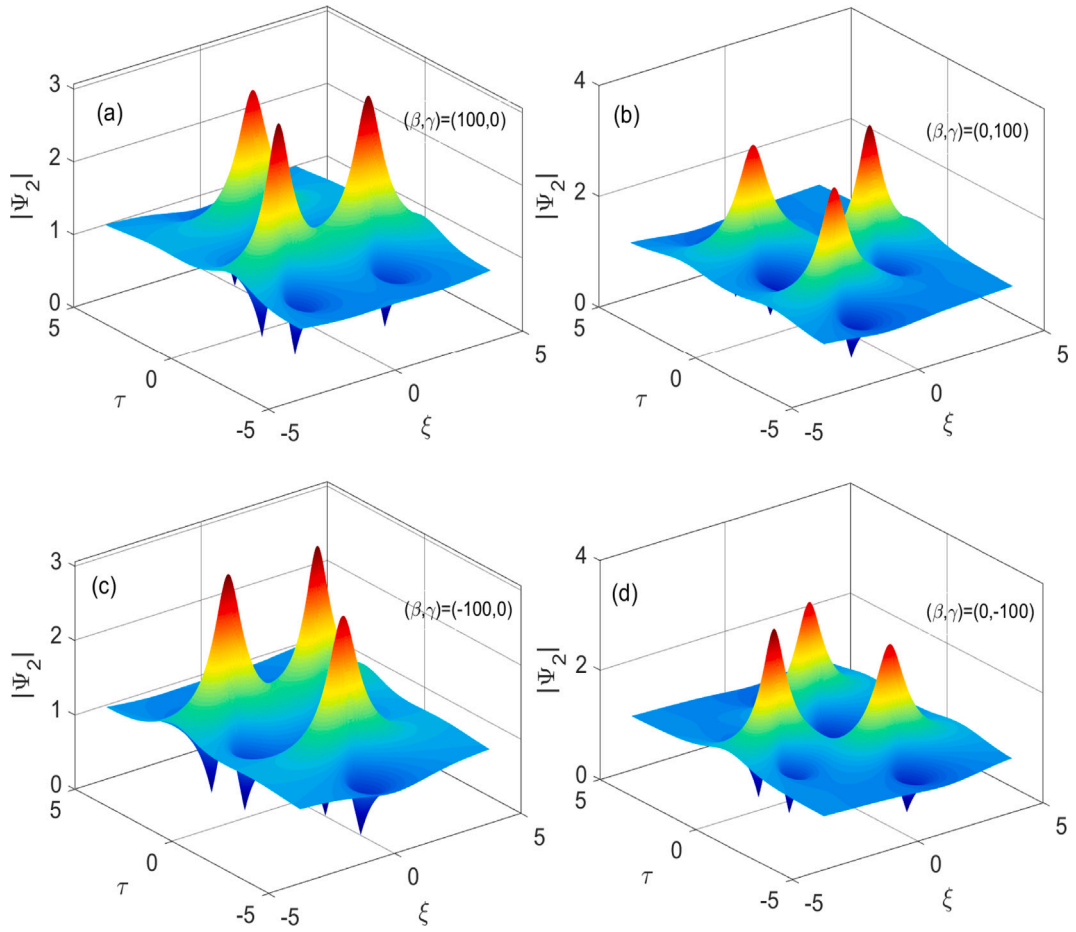

Fig. 10. The 3D behavior of the rogue wave triplets $|\Psi_2|$ with respect to ξ and τ for (a) $\beta = 100$ and $\gamma = 0$, (b) $\beta = 0$ and $\gamma = 100$, (c) $\beta = -100$ and $\gamma = 0$, and (d) $\beta = 0$ and $\gamma = -100$. The other parameters are $r = 1$, $q = 2$, and $k = 2.5$.

representations shown in Figs. 10 and 11, respectively. The ion acoustic rogue wave triplets resemble a second-order rogue wave that consist of three peaks forming a triangular pattern. To represent a qualitative sketch of the rogue waves structure that is symmetrical about the ξ-axis, the shift is controlled by setting the physical free parameters β and γ (as described in Eqs. (33)–(35)). The intensity profiles, as depicted in Figs. 10(a) and 10(b), are plotted for a given set of values of the physical free parameters, namely $(\beta, \gamma) = (100, 0)$ and $(\beta, \gamma) = (0, 100)$, respectively. The amplitude of the rogue wave triplets at $(\beta, \gamma) = (100, 0)$ is found to be slightly larger than the amplitude at $(\beta, \gamma) = (0, 100)$. It is interesting to observe that the triangular pattern of the rogue wave rotates anti-clockwise on the (ξ, τ) plane, as illustrated in Figs. 10(a) and 10(b). Furthermore, the variation in the absolute of ion acoustic rogue wave triplet profiles for negative β and γ are also depicted in Figs. 10(c) and 10(d). These figures reveal that the rogue wave triplets also have an anti-clockwise orientation. The rogue wave triplets show a larger magnitude for positive (negative) values of β at $\gamma = 0$ compared to positive (negative) values of γ at $\beta = 0$. Fig. 11 displays the 2D representation of the rogue wave triplets for varying free parameters, namely β and γ. This figure also indicates the triangular pattern of the rogue waves. The oval-shaped red color regions in Fig. 11(a) distinctly indicate the peaks of the rogue wave triplets, with the bottom ovals regions exhibiting larger magnitudes than the top oval $\beta = 100$ and $\gamma = 0$. The 2D representation of rogue wave triplets shown in Fig. 11(b) for $\beta = 0$ and $\gamma = 100$ indicates that the oval region on the right has a larger magnitude compared to the ovals regions on the left. The inverse behavior of the rogue wave triplets shown in Figs. 11(c) and 11(d) for negative values of the free parameters ($\beta = -100$ and $\gamma = -100$) can be observed when compared with Figs. 10(a) and 10(b). One can immediately draw the conclusion that a 180° orientation is observed when compare the figures 10(a) and 10(b) with Figs. 11(c) and 11(d), respectively.

Fig. 12 illustrates examples of the rogue wave triplets for the parameters $\beta = 100, 50, 15, 0$ at $\gamma = 0$. A triangular pattern featuring three peaks is shown for $\beta = 100$, as depicted in (a). The three peaks can also be observed when β is adjusted to 50 (see Fig. 11(b)). For the scenario with $\beta = 15$, the peaks move closer together, as illustrated in Fig. 12(c). Upon decreasing the parameter β to zero, the rogue wave triplets are fully converted into second-order rogue waves, commonly known as super freak waves. It can be concluded that the rogue wave triplets become super freak waves under the conditions $\beta = 0$ and $\gamma = 0$. In the context of MI in IAWs, rogue wave triplets typically manifest as three distinct localized waves arranged in triangular pattern with their amplitude and peak separation influenced by the free parameters β and γ. As the parameters approach specific values, namely $\beta = 0$ and $\gamma = 0$, the rogue wave triplets merge into a single, highly localized wave with an extremely high amplitude, often referred to as a super freak wave. This transition emphasizes the critical role of free plasma parameters in shaping the instability and nonlinear IAW dynamics. As illustrated in Fig. 13, the intensity profiles of rogue wave triplets are plotted against ξ at $\tau = 1$ for different values of the parameters of both the distribution functions, namely (r, α) and (q, q_n). The contributions of nonthermal electrons α and spectral index r to the rogue wave analysis are analogous in both distribution functions. However, the peaks of the rogue wave at approximately $\xi = 2.5$ are larger for the generalized distribution function compared to the nonextensive nonthermal distribution, as illustrated in Fig. 13(a). As shown in Fig. 13(b), a similar trend is evident for the nonextensive parameter q_n and

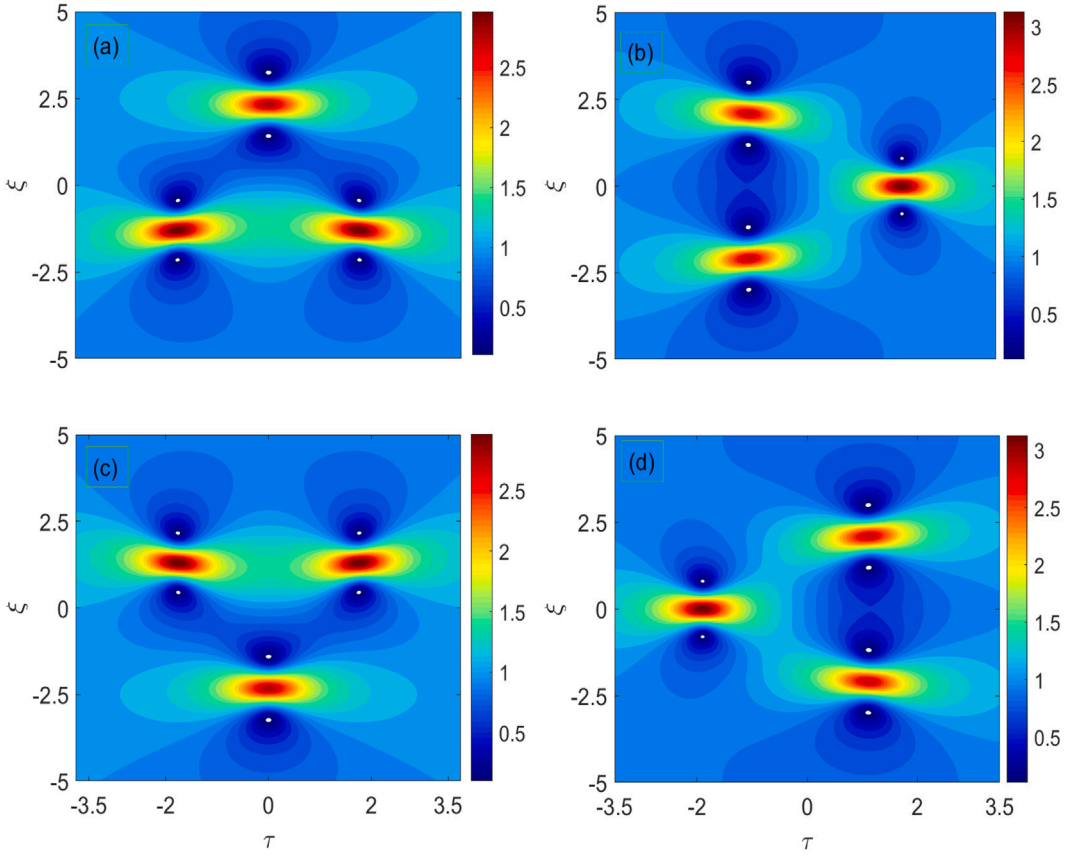

Fig. 11. The 2D behavior of the rogue wave triplets $|\Psi_2|$ with respect to ξ and τ for (a) $\beta = 100$ and $\gamma = 0$, (b) $\beta = 0$ and $\gamma = 100$, (c) $\beta = -100$ and $\gamma = 0$, and (d) $\beta = 0$ and $\gamma = -100$. The other parameters are $r = 1$, $q = 2$, and $k = 2.5$.

the spectral index q in the nonextensive nonthermal distribution and the generalized distribution function, respectively.

5. Envelope solitons

The NLSE (19) exhibits integrability and supports exact localized solutions such as envelope solitons [63–65]. These solutions are expressed as $\Psi_{D,B}(\xi,\tau) = \rho_{D,B}(\xi,\tau)e^{i\Theta_{D,B}(\xi,\tau)}$, where $\Theta_{D,B}$ represents the nonlinear phase shift and $\rho_{D,B}$ is the envelope amplitude for dark and bright solitons. The nature of the solitons depends on the signs of the dispersion P and nonlinear Q coefficients of NLSE [64,65]. For $PQ < 0$, the system corresponds to dark soliton with large wavelengths or small wavenumbers in the modulationally stable region (particularly for carrier wavenumber $k = 1.5$), as illustrated earlier in Fig. 3. An analytical equation describing such dark solitons is provided in Ref. [35] as follows

$$\rho_D(\xi,\tau) = \Psi_0\left[1 - d^2\mathrm{sech}^2\left(\frac{\xi - V\tau}{L}\right)\right]^{1/2},$$
$$\Theta_D = \frac{1}{2P}\left[V\xi - \left(\frac{V^2}{2} - 2PQ\Psi_0\right)\tau\right]$$

The parameter Ψ_0 represents an asymptotic value of the electrostatic potential amplitude, V is the constant propagation speed, and L denotes the soliton width. The positive constant d determines the depth of the void, with $d = 1$ and $k = 1.5$ (consistent with the P/Q profiles) corresponding to dark solitons, as illustrated in Fig. 14(a) and (b). The dark soliton profiles are clearly illustrated for $\tau = 0.1$ and $\tau = 1.0$, respectively. The red line denotes the reference level where $\Psi_D, B = 0$, which is a baseline for visualization of the amplitude characteristic of dark/bright solitons. In the modulationally stable region, dark solitons emerge as localized envelope voids (holes) that propagate within the plasma. These solitons represent localized depressions in wave amplitude rather than peaks, distinguishing them from bright solitons. Consequently, the dark solitons are a prevalent form of electrostatic wavepacket in plasmas, arising due to the self-modulation.

Conversely, when the dispersion P and nonlinear Q have the same sign (i.e., $PQ > 0$), corresponding to shorter wavelengths or higher wavenumbers (as already illustrated in Fig. 3), bright-type solitons emerge. An analytical equation for bright solitons is given in [35,64–66]

$$\rho_B(\xi,\tau) = \Psi_0 sech\left[\frac{\xi - V\tau}{L}\right],$$
$$\Theta_B = \frac{1}{2P}\left[V\xi - \left(\frac{V^2}{2} + \Omega\right)\tau\right]$$

where Ω denotes the oscillation frequency of the bell-shaped envelope solitons when $V = 0$. Note that such excitations are observed in optical fibers and bear a qualitative resemblance to bright pulses in the field of nonlinear optics [67]. The soliton width L exhibits a strong dependence on the amplitude, given by the expression $(2|P|/|Q|)^{1/2}/\Psi_0$. It is important to emphasize that bright solitons emerge under the same conditions required for the occurrence of MI, specifically when $PQ > 0$ (usually P/Q profiles are evaluated for $k = 2.5$ or above), as shown in Fig. 15 (a) and (b). Such bright envelope solitons are commonly observed in space plasmas [66,68].

6. Conclusion

To summarize, we have explored the MI, dark/bright solitons, and rogue wave triplet structures, taking into account the various parameters associated with the (r,q) generalized and q_n-nonextensive nonthermal distribution functions. This paper conducts a thorough

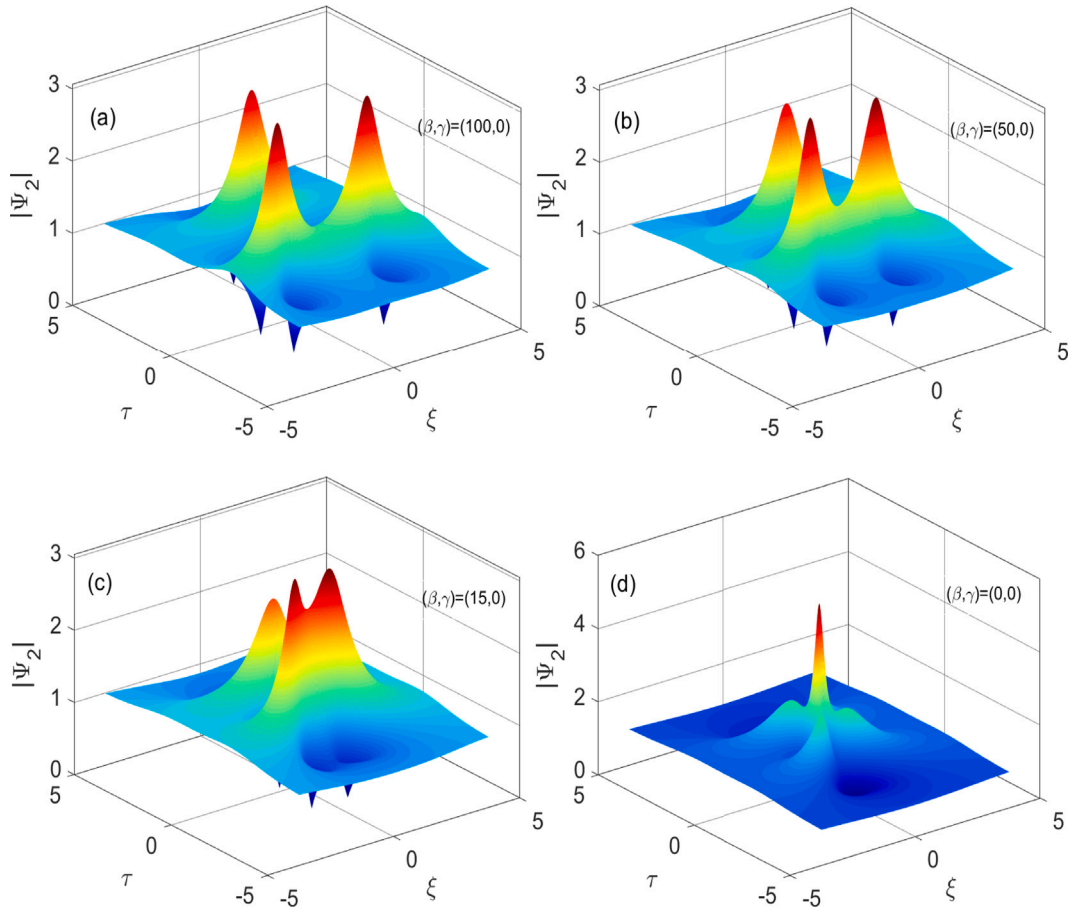

Fig. 12. The 3D behavior of the rogue wave triplets $|\Psi_2|$ with respect to ξ and τ for (a) $\beta = 100$ and $\gamma = 0$, (b) $\beta = 50$ and $\gamma = 0$, (c) $\beta = 15$ and $\gamma = 0$, and (d) $\beta = 0$ and $\gamma = 0$. The other parameters are $r = 1$, $q = 2$, and $k = 2.5$.

comparison of IAWs, aligning the current findings using the (r, q) distribution function with earlier results by Bouzit (2015) based on the nonextensive nonthermal velocity distribution, which are reproduced herein. In this context, the fluid model that incorporates the continuity, velocity and Poisson equations is condensed to a NLSE by employing the reductive perturbation technique. The carrier frequency approaches unity upon increasing the wavenumber, signifying the high-frequency regime where it becomes less sensitive to further increases in k, while the group velocity slows down at large wavenumbers, indicating the wave dissipation in the plasma. Based on the criteria for MI, characterized by the ratio of the coefficients of the NLSE (P/Q), the stable and unstable regions have been precisely identified for different distribution functions where the onset of MI arises. It has been noted that the stable region defining the dark soliton varies inversely with the spectral indices (r, q), and its effect on the dark soliton is more significant at lower end of wavenumber (k). However, the effect of the indices in the unstable region characterizing the bright soliton is minimal at high end of k. A comparison study is being made between these results and those obtained for the nonextensive nonthermal velocity distribution. The nonthermal electrons α and the nonextensive parameter q_n have significantly influenced the behavior of dark and bright solitons. A key component of the plasma system's behavior under consideration is the shift from a stable to an unstable regime that contributes to the possibility of rogue wave formation, in which the localized waves of large amplitude can emerge suddenly. This shift in soliton instability analysis demonstrates the significant influence of nonlinearity in the generation of extreme wave events, such as rogue waves, often driven by the MI. It has also been noted that the growth rate of MI exhibits a strong dependence on both the spectral indices of the generalized distribution function and the generation of nonthermal electrons in the nonextensive nonthermal distribution function. The unstable region, in terms of the growth rate, increases significantly with the presence of nonthermal electrons and the nonextensive parameter, rather than being influenced by the spectral indices of the generalized distribution function. The generalized (r, q) distribution function effectively suppresses growth rates in the small k regime, and therefore reducing energy available for large-scale instabilities. Conversely, the nonextensive nonthermal distribution enhances the growth rate suppression in the large k regime, suggesting stronger damping of shortwavelength instabilities. These distributions uniquely influence MI dynamics, with the (r, q) distribution stabilizing long-wavelength modes and the nonextensive nonthermal distribution damping short-wavelength modes.

In addition, the characteristics of the rogue wave triplets have also been explored. We have provided an in-depth exploration of the 3D visuals of the first-order rogue waves and rogue wave triplets. A qualitative sketch of the rogue wave triplets arranged in a triangular pattern has been acquired, based on the physical free parameters β and γ. Moreover, the rogue wave triplets can be regarded as super freak waves when the physical free parameters are both equal to zero ($\beta = 0$ and $\gamma = 0$). In conclusion, both the (r, q) generalized distribution function and the q_n-nonextensive nonthermal velocity distribution function provide valuable insights that substantially enhance our understanding of IAWs in nonthermal plasma environments. Moreover, we have comprehensively examined the existence domains of both dark and bright solitons, which are associated with modulationally unstable and stable regimes of IAWs, respectively. Our analysis further explores the conditions under which these solitons emerge, describing their distinct characteristics in relation to the stability properties of the wave dynamics. The influence of an external magnetic field on the dynamics

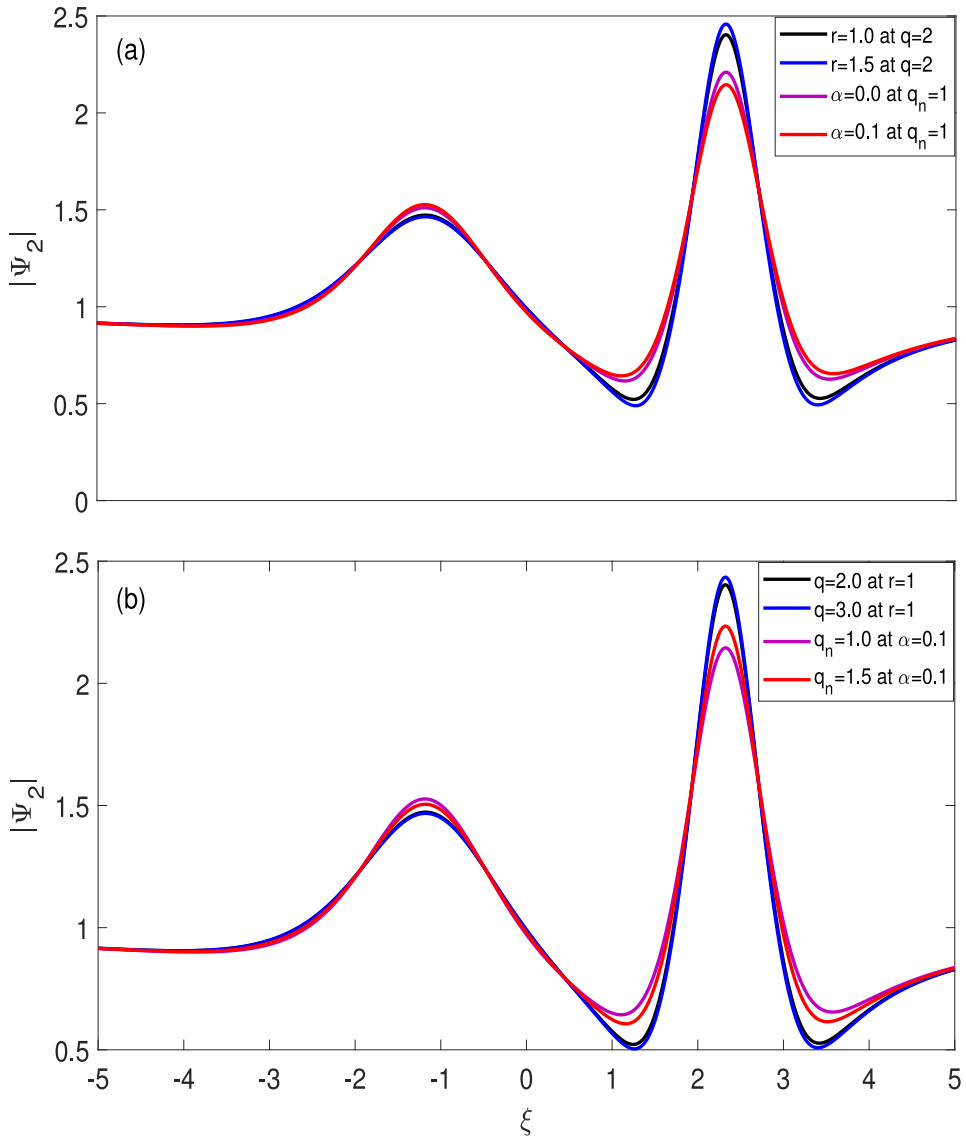

Fig. 13. The 1D behavior of the rogue wave triplets for the generalized (r, q) and q_n-nonextensive distribution functions with respect to spatial coordinate ξ for different values of (a) the spectral index $r(= 1.0, 1.5)$ at $q = 2$ and $\alpha(= 0.05, 0.07)$ at $q_n = 0.9$, and (b) the spectral index $q(= 2.0, 3.0)$ at $r = 1.0$ and $q_n = (0.9, 1.0)$ at $\alpha = 0.05$.

of MI and rogue wave triplets is a significant area of research in dense plasma environments. This particular aspect is beyond the focus of our present study and could serve as a subject for future study. Future work should also focus on implementing numerical methods to solve the NLSE, which will help in validating and expanding the analytical results presented in this study. This combination of analytical and numerical approaches will provide a more comprehensive understanding of the problem and its solutions.

CRediT authorship contribution statement

Abdullah Khan: Writing – original draft, Formal analysis, Data curation, Conceptualization. **Aamir Farooq:** Writing – review & editing, Validation, Formal analysis. **A.A. Abid:** Writing – original draft, Visualization, Validation, Supervision, Formal analysis. **Malik Sadam Hussain:** Validation, Methodology, Formal analysis, Data curation. **Wen-Xiu Ma:** Writing – review & editing, Supervision, Investigation. **Shaaban M. Shaaban:** Investigation, Writing – review & editing.

Declaration of competing interest

The authors declare that they have no known competing financial interests or personal relationships that could have appeared to influence the work reported in this paper.

Acknowledgments

The author, Abdullah Khan, greatly acknowledges the postdoctoral fellowship supported by Zhejiang Normal University, China under Grant No. YS304023906. The authors extend their appreciation to the Deanship of Scientific Research at Northern Border University, Arar, KSA for funding this research work through the project number "NBU-FPEJ-2025-289-02".

Data availability

No data was used for the research described in the article.

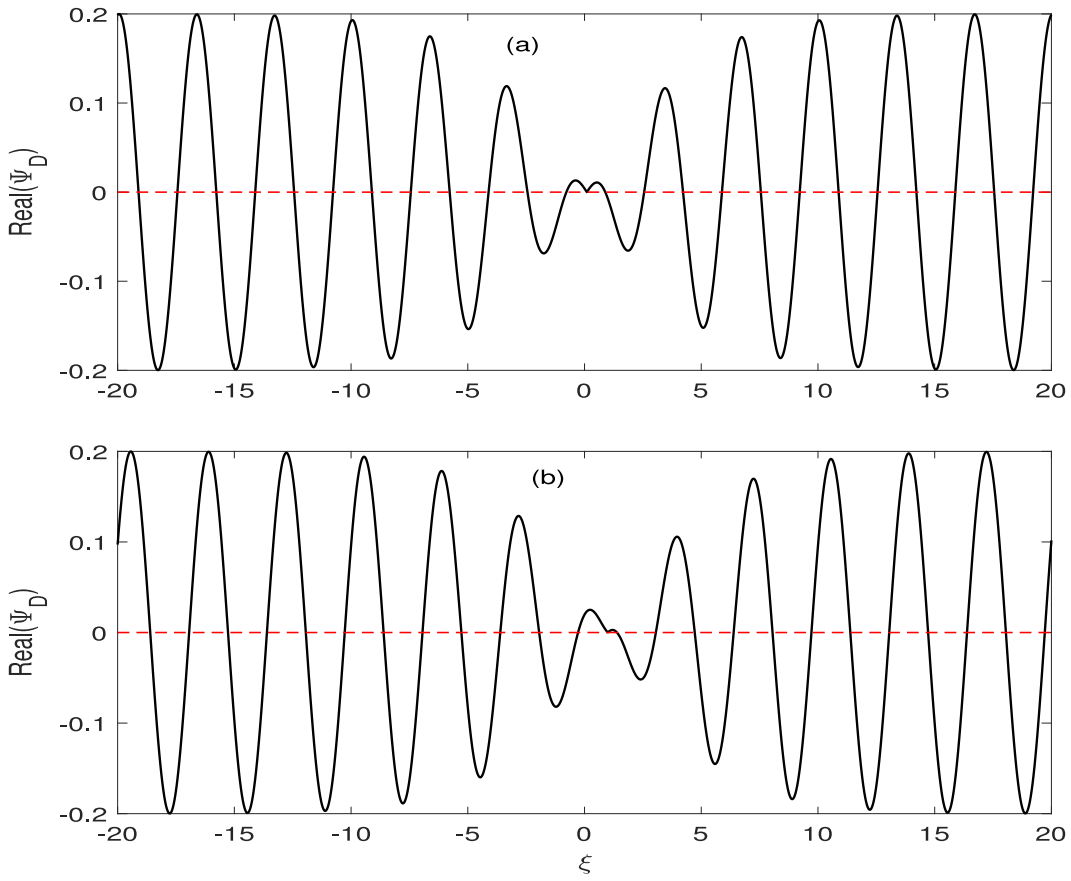

Fig. 14. Variation of the dark envelope solitons Real(Ψ_D) versus the spatial coordinate (ξ) in the regime $PQ < 0$ for different values of the temporal coordinate (a) $\tau = 0.1$ and (b) $\tau = 1.0$ at $d = 1$ and $V = 1$.

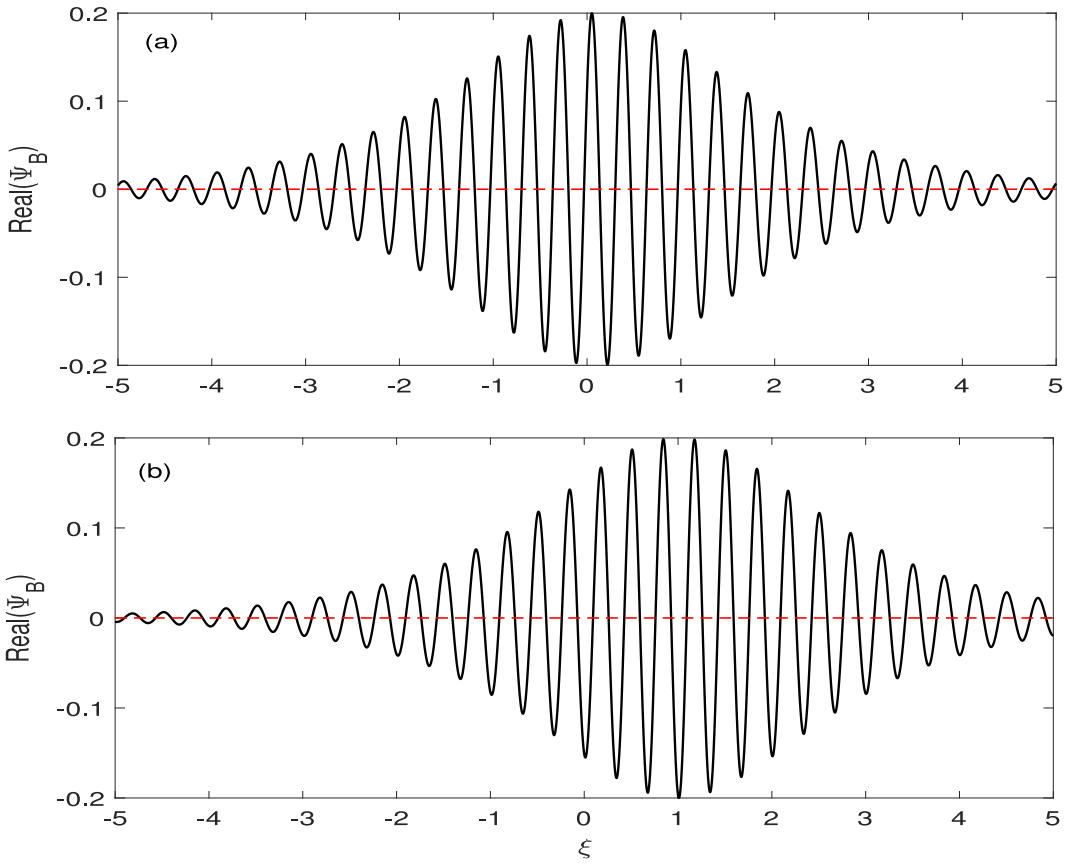

Fig. 15. Variation of the bright envelope solitons Real(Ψ_B) versus the spatial coordinate (ξ) in the regime $PQ > 0$ for different values of the temporal coordinate (a) $\tau = 0.1$ and (b) $\tau = 1.0$ at $d = 1$ and $V = 1$.

References

[1] Agrawal GP. Modulation instability induced by cross-phase modulation. Phys Rev Lett 1987;59(8):880.
[2] Melville W. The instability and breaking of deep-water waves. J Fluid Mech 1982;115:165–85.
[3] Galeev A, Sagdeev R, Sigov YS, Shapiro V, Shevchenko V. Nonlinear theory of the modulation instability of plasma waves. Sov J Plasma Phys (Engl Transl); (United States) 1975;1(1).
[4] Bhat IA, Mithun T, Malomed B, Porsezian K. Modulational instability in binary spin-orbit-coupled Bose-Einstein condensates. Phys Rev A 2015;92(6):063606.
[5] Osborne AR. Nonlinear ocean wave and the inverse scattering transform. In: Scattering. Elsevier; 2002, p. 637–66.
[6] Watanabe S. Self-modulation of a nonlinear ion wave packet. J Plasma Phys 1977;17(3):487–501.
[7] Chawla J, Mishra M, Tiwari R. Modulational instability of ion-acoustic waves in electron–positron–ion plasmas. Astrophys Space Sci 2013;347:283–92.
[8] Jain S, Mishra M. Arbitrary amplitude ion-acoustic solitons in two-electron temperature warm ion plasma. Astrophys Space Sci 2013;346:395–407.
[9] Kourakis I, Esfandyari-Kalejahi A, Mehdipoor M, Shukla P. Modulated electrostatic modes in pair plasmas: Modulational stability profile and envelope excitations. Phys Plasmas 2006;13(5).
[10] Nejoh Y. The effect of the ion temperature on large amplitude ion-acoustic waves in an electron–positron–ion plasma. Phys Plasmas 1996;3(4):1447–51.
[11] Ghosh UN, Saha A, Pal N, Chatterjee P. Dynamic structures of nonlinear ion acoustic waves in a nonextensive electron–positron–ion plasma. J Theor Appl Phys 2015;9:321–9.
[12] Tiwari R, Kaushik A, Mishra M. Effects of positron density and temperature on ion acoustic dressed solitons in an electron–positron–ion plasma. Phys Lett A 2007;365(4):335–40.
[13] Saha A, Pal N, Chatterjee P. Dynamic behavior of ion acoustic waves in electron-positron-ion magnetoplasmas with superthermal electrons and positrons. Phys Plasmas 2014;21(10).
[14] Jehan N, Salahuddin M, Saleem H, Mirza AM. Modulation instability of low-frequency electrostatic ion waves in magnetized electron-positron-ion plasma. Phys Plasmas 2008;15(9).
[15] Kharif C, Pelinovsky E, Slunyaev A. Rogue waves in the ocean. Springer Science & Business Media; 2008.
[16] Toffoli A, Waseda T, Houtani H, Kinoshita T, Collins K, Proment D, et al. Excitation of rogue waves in a variable medium: An experimental study on the interaction of water waves and currents. Phys Rev E— Stat Nonlinear, Soft Matter Phys 2013;87(5):051201.
[17] Chabchoub A, Hoffmann N, Onorato M, Akhmediev N. Super rogue waves: observation of a higher-order breather in water waves. Phys Rev X 2012;2(1):011015.
[18] Benjamin TB, Feir JE. The disintegration of wave trains on deep water Part 1. Theory. J Fluid Mech 1967;27(3):417–30.
[19] Zakharov VE. Stability of periodic waves of finite amplitude on the surface of a deep fluid. J Appl Mech Tech Phys 1968;9(2):190–4.
[20] Akhmediev N, Ankiewicz A, Taki M. Waves that appear from nowhere and disappear without a trace. Phys Lett A 2009;373(6):675–8.
[21] Akhmediev N, Ankiewicz A, Soto-Crespo JM. Rogue waves and rational solutions of the nonlinear Schrödinger equation. Phys Rev E— Stat Nonlinear, Soft Matter Phys 2009;80(2):026601.
[22] Onorato M, Residori S, Bortolozzo U, Montina A, Arecchi F. Rogue waves and their generating mechanisms in different physical contexts. Phys Rep 2013;528(2):47–89.
[23] Shrira VI, Geogjaev VV. What makes the Peregrine soliton so special as a prototype of freak waves? J Engrg Math 2010;67:11–22.
[24] Chabchoub A, Fink M. Time-reversal generation of rogue waves. Phys Rev Lett 2014;112(12):124101.
[25] Kibler B, Fatome J, Finot C, Millot G, Dias F, Genty G, et al. The Peregrine soliton in nonlinear fibre optics. Nat Phys 2010;6(10):790–5.
[26] Chabchoub A, Hoffmann N, Akhmediev N. Rogue wave observation in a water wave tank. Phys Rev Lett 2011;106(20):204502.
[27] Bailung H, Sharma S, Nakamura Y. Observation of peregrine solitons in a multicomponent plasma with negative ions. Phys Rev Lett 2011;107(25):255005.
[28] Hirota R. The direct method in soliton theory. (155). Cambridge University Press; 2004.
[29] Matveev VB, Salle MA. Darboux transformations and solitons. Springer Ser Nonlinear Dyn 1991.
[30] Sarkar J, Saha A. Role of polarized force on dust-acoustic structures in the presence of suprathermal electrons. Phys Fluids 2024;36(4).
[31] Khan A, Abid AA, Khan M, Kengne E. Quantifying the effects of generalized (r, q) distribution function on modulational instability and rogue wave of electron acoustic solitons. Phys Scr 2024.

[32] Saha A, Banerjee S. Dynamical systems and nonlinear waves in plasmas. CRC Press; 2021.
[33] Mamun A. Arbitrary amplitude dust-acoustic solitary structures in athree-component dusty plasma. Astrophys Space Sci 1999;268:443–54.
[34] Maji TK, Ghorui MK, Saha A, Chatterjee P. Oblique interaction of ion-acoustic solitary waves in epi plasmas. Braz J Phys 2017;47:295–301.
[35] Kourakis I, Shukla PK. Electron-acoustic plasma waves: oblique modulation and envelope solitons. Phys Rev E 2004;69(3):036411.
[36] Sultana S, Schlickeiser R, Elkamash I, Kourakis I. Dissipative high-frequency envelope soliton modes in nonthermal plasmas. Phys Rev E 2018;98(3):033207.
[37] Schamel H. Kinetic theory of phase space vortices and double layers. Phys Scr 1982;1982(T2A):228.
[38] Zaghbeer S, Salah H, Sheta N, El-Shewy E, Elgarayh A. Effect of nonextensive electron and ion on dust acoustic rogue waves in dusty plasma of opposite polarity. Astrophys Space Sci 2014;353:493–500.
[39] Qureshi M, Shah H, Murtaza G, Schwartz S, Mahmood F. Parallel propagating electromagnetic modes with the generalized (r, q) distribution function. Phys Plasmas 2004;11(8):3819–29.
[40] Zaheer S, Murtaza G, Shah H. Some electrostatic modes based on non-Maxwellian distribution functions. Phys Plasmas 2004;11(5):2246–55.
[41] Shah K, Qureshi M, Masood W, Shah H. Electron acoustic nonlinear structures in planetary magnetospheres. Phys Plasmas 2018;25(4).
[42] Latora V, Rapisarda A, Tsallis C. Non-Gaussian equilibrium in a long-range Hamiltonian system. Phys Rev E 2001;64(5):056134.
[43] Latora V, Rapisarda A, Tsallis C. Fingerprints of nonextensive thermodynamics in a long-range Hamiltonian system. Phys A 2002;305(1–2):129–36.
[44] Kumar Samanta U, Saha A, Chatterjee P. Bifurcations of nonlinear ion acoustic travelling waves in the frame of a Zakharov-Kuznetsov equation in magnetized plasma with a kappa distributed electron. Phys Plasmas 2013;20(5).
[45] Bouzit O, Tribeche M, Bains A. Modulational instability of ion-acoustic waves in plasma with a q-nonextensive nonthermal electron velocity distribution. Phys Plasmas 2015;22(8).
[46] Parks G, Lee E, Lin N, Mozer F, Wilber M, Dandouras I, et al. Solitary electromagnetic pulses detected with super-Alfvénic flows in Earth's geomagnetic tail. Phys Rev Lett 2007;98(26):265001.
[47] Masood W, Schwartz S, Maksimovic M, Fazakerley A. Electron velocity distribution and lion roars in the magnetosheath. In: Annales geophysicae, vol. 24, (6):Copernicus Publications Göttingen, Germany; 2006, p. 1725–35.
[48] Kouser S, Shah K, Qureshi M, Shah H. Nonlinear ion-acoustic waves in e–p–i plasmas with (r, q) distributed electrons and positrons. AIP Adv 2020;10(5).
[49] Shabbir S, Khan M, Kamran M. Effect of generalized (r, q)-distributed electrons on ion polytropic coefficient in bounded plasmas. J Phys A 2022;55(26):265202.
[50] Bains A, Tribeche M, Gill T. Modulational instability of ion-acoustic waves in a plasma with a q-nonextensive electron velocity distribution. Phys Plasmas 2011;18(2).
[51] Verheest F. Ambiguities in the tsallis description of non-thermal plasma species. J Plasma Phys 2013;79(6):1031–4.
[52] Khalid S, Qureshi M, Masood W. Nonlinear kinetic Alfven waves in space plasmas with generalized (r, q) distribution. Astrophys Space Sci 2018;363(10):216.
[53] Williams G, Kourakis I, Verheest F, Hellberg MA. Re-examining the Cairns-Tsallis model for ion acoustic solitons. Phys Rev E— Stat Nonlinear, Soft Matter Phys 2013;88(2):023103.
[54] Cairns R, Mamum A, Bingham R, Boström R, Dendy R, Nairn C, et al. Electrostatic solitary structures in non-thermal plasmas. Geophys Res Lett 1995;22(20):2709–12.
[55] Sabry R. Modulation instability of ion thermal waves in a pair-ion plasma containing charged dust impurities. Phys Plasmas 2008;15(9).
[56] Tolba R, Moslem W, Sabry R. Modulated dust-ion-acoustic waves result from Earth's magnetosphere and lunar ionosphere interactions. Phys Fluids 2024;36(3).
[57] Bains AS, Tribeche M, Gill TS. Modulational instability of electron-acoustic waves in a plasma with a q-nonextensive electron velocity distribution. Phys Lett A 2011;375(20):2059–63.
[58] Panwar A, Ryu C-M. Modulational instability and associated rogue structures of slow magnetosonic wave in Hall magnetohydrodynamic plasmas. Phys Plasmas 2014;21(6).
[59] Emmanuel K, Wuming L. Dissipative ion-acoustic solitons in ion-beam plasma obeying a κ-distribution. AIP Adv 2020;10(4).
[60] Ankiewicz A, Kedziora DJ, Akhmediev N. Rogue wave triplets. Phys Lett A 2011;375(28–29):2782–5.
[61] Chabchoub A, Akhmediev N. Observation of rogue wave triplets in water waves. Phys Lett A 2013;377(38):2590–3.
[62] Dubard P, Gaillard P, Klein C, Matveev V. On multi-rogue wave solutions of the NLS equation and positon solutions of the KdV equation. Eur Phys J Spec Top 2010;185(1):247–58.
[63] Dauxois T, Peyrard M. Physics of solitons. Cambridge University Press; 2006.
[64] Fedele R, Schamel H. Solitary waves in the Madelung's fluid: Connection between the nonlinear Schrödinger equation and the Korteweg-de Vries equation. Eur Phys J B- Condens Matter Complex Syst 2002;27:313–20.
[65] Fedele R, Schamel H, Shukla PK. Solitons in the Madelung's fluid. Phys Scr 2002;2002(T98):18.
[66] Kourakis I, Shukla P. Exact theory for localized envelope modulated electrostatic wavepackets in space and dusty plasmas. Nonlinear Process Geophys 2005;12(3):407–23.
[67] Kivshar YS, Agrawal GP. Optical solitons: from fibers to photonic crystals. Academic Press; 2003.
[68] Pickett J, Gurnett D, Menietti J, LeDocq M, Scudder J, Frank L, et al. Plasma waves observed during cusp energetic particle events and their correlation with Polar and Akebono satellite and ground data. Adv Space Res 1999;24(1):23–33.